

**ISTANBUL TECHNICAL UNIVERSITY ★ GRADUATE SCHOOL OF SCIENCE**  
**ENGINEERING AND TECHNOLOGY**

**CHEMICAL DEINTERCALATION AND STABILITY INVESTIGATION OF  
NANOSIZED C/Li<sub>2</sub>MnSiO<sub>4</sub> CATHODE MATERIAL WITH DIFFERENT  
ELECTROLYTES**

**M.Sc. THESIS**

**Ekin EŐEN**

**Department of Nanoscience and Nanoengineering**  
**Nanoscience and Nanoengineering Programme**

**MAY 2015**



**ISTANBUL TECHNICAL UNIVERSITY ★ GRADUATE SCHOOL OF SCIENCE**  
**ENGINEERING AND TECHNOLOGY**

**CHEMICAL DEINTERCALATION AND STABILITY INVESTIGATION OF  
NANOSIZED C/Li<sub>2</sub>MnSiO<sub>4</sub> CATHODE MATERIAL WITH DIFFERENT  
ELECTROLYTES**

**M.Sc. THESIS**

**Ekin EŐEN**  
**(513121004)**

**Department of Nanoscience and Nanoengineering**  
**Nanoscience and Nanoengineering Programme**

**Thesis Advisor: Prof. Dr. Figen KADIRGAN**

**MAY 2015**



**İSTANBUL TEKNİK ÜNİVERSİTESİ ★ FEN BİLİMLERİ ENSTİTÜSÜ**

**C/Li<sub>2</sub>MnSiO<sub>4</sub> KATOT MALZEMESİNİN KİMYASAL DEİTERKALASYONU  
VE FARKLI ELEKTROLİTLER İLE KARARLILIĞININ İNCELENMESİ**

**YÜKSEK LİSANS TEZİ**

**Ekin EŞEN  
(513121004)**

**Nanobilim ve Nanomühendislik Anabilim Dalı  
Nanobilim ve Nanomühendislik Programı**

**Tez Danışmanı: Prof. Dr. Figen KADIRGAN**

**MAYIS 2015**







*To my mother, brother & friends*



## **FOREWORD**

I would like to express my sincere appreciation and thanks to my supervisor, Prof. Dr. Figen KADIRGAN for her continuous encouragement, guidance, motivation, and immense knowledge.

I am also thankful to my colleagues Michal Swietoslawski, Agnieszka Chojnacka, Monika Bakierska, and Malgorzata Rutkowska for their enthusiasm to share the knowledge as well as their collaborative and friendly attitudes during my exchange year.

I would especially like to thank my friends Rıdvan Ergun, Ayşegül Develiođlu, Uđur Dađlı, Ömercan Susam, Mojgan Laki, Elbruz Murat Baba, Cengizhan Karbay and İpek Kuru for the fun and quality time.

Lastly, and most importantly, I wish to thank my mother and my brother for their infinite love and support.

May 2015

Ekin EŞEN  
Chemist



## TABLE OF CONTENTS

	<u>Page</u>
<b>FOREWORD</b> .....	<b>ix</b>
<b>ABBREVIATIONS</b> .....	<b>xiii</b>
<b>LIST OF TABLES</b> .....	<b>xv</b>
<b>LIST OF FIGURES</b> .....	<b>xvii</b>
<b>SUMMARY</b> .....	<b>xix</b>
<b>ÖZET</b> .....	<b>xxi</b>
<b>1 . INTRODUCTION</b> .....	<b>1</b>
<b>2 . BATTERIES</b> .....	<b>3</b>
2.1 Rechargeable Batteries .....	3
2.1.1 Lithium ion batteries .....	5
2.1.2 Cathode materials .....	6
<b>3 . PRINCIPLES OF CHARACTERIZATION METHODS</b> .....	<b>9</b>
3.1 Thermogravimetric Analysis (TGA) .....	9
3.2 X-ray Powder Diffraction (XRD) .....	9
3.3 X-ray Photoelectron Spectroscopy (XPS) .....	10
3.4 Conductivity Measurement .....	11
<b>4 . EXPERIMENTAL PART</b> .....	<b>15</b>
4.1 Production of Pristine $\text{Li}_2\text{MnSiO}_4$ Powder .....	15
4.1.1 Preparation of the precursor .....	15
4.1.2 Calcination of the precursor gel .....	15
4.1.3 Removal of the undesired carbon shell from the calcined sample .....	16
4.1.4 Reduction .....	16
4.2 Production of C/ $\text{Li}_2\text{MnSiO}_4$ Composites .....	17
4.2.1 Conductive carbon layer (CCL) coating .....	17
4.2.2 Pyrolysis .....	17
4.3 Characterization of the Cathode Materials .....	18
4.3.1 Thermogravimetric analysis (TGA) and mass spectrometry (MS) .....	18
4.3.2 Preparation of the reference XRD patterns for $\text{Li}_2\text{MnSiO}_4$ , $\text{LiMnSiO}_4$ and $\text{MnSiO}_4$ .....	18

4.3.3 X-ray powder diffraction (XRD).....	20
4.3.4 X-ray photoelectron spectroscopy (XPS) .....	20
4.3.5 Conductivity and activation energy .....	21
4.3.6 Differential scanning calorimetry (DSC).....	21
4.4 Preparation of the Electrolyte Solutions .....	22
4.5 Chemical Delithiation .....	22
4.6 Electrochemical Oxidation/Delithation .....	24
4.6.1 Assembling of coin cell type batteries .....	25
4.6.2 Disassembling of coin cell type batteries.....	26
<b>5 . RESULTS AND DISCUSSIONS .....</b>	<b>27</b>
5.1 Comparison of the XRD Patterns of Synthesized Cathode Materials.....	27
5.2 Conductivity and Activation Energy Results .....	28
5.3 TGA Results.....	30
5.4 Chemical Oxidation/Delithation Results .....	32
5.4.1 XRD results .....	33
5.4.2 XPS results.....	38
5.5 Electrochemical Oxidation/Delithation Results.....	39
5.5.1 Determination of the optimum carbon percentage for the cathode materials in the batteries prepared using LiPF <sub>6</sub> electrolyte solutions .....	40
5.5.2 Comparison of the electrolyte solution performances.....	45
5.5.3 XPS result of the fully charged cathode material .....	47
5.6 DSC Results .....	47
<b>6. CONCLUSIONS.....</b>	<b>49</b>
<b>7. REFERENCES .....</b>	<b>51</b>
<b>CURRICULUM VITAE .....</b>	<b>55</b>

## ABBREVIATIONS

<b>HEVs</b>	: Hybrid Vehicles
<b>EVs</b>	: Electric Vehicles
<b>LA</b>	: Lead Acid Batteries
<b>NiMH</b>	: Nickel Metal Hydride Batteries
<b>Li-ion</b>	: Lithium Ion Batteries
<b>C/Li<sub>2</sub>MnSiO<sub>4</sub></b>	: Lithium Manganese Silicate Nanocomposites
<b>TGA</b>	: Thermogravimetric Analysis
<b>XRD</b>	: X-ray Powder Diffraction
<b>XPS</b>	: X-ray Photoelectron Spectroscopy
<b>BE</b>	: Binding Energy (for XPS)
<b>DSC</b>	: Differential Scanning Calorimetry
<b>PMA</b>	: Pyromellitic Acid
<b>PNVF</b>	: Poly N-vinylformamide
<b>EC</b>	: Electrical Conductivity
<b>QMS</b>	: Quadripole Mass Spectrometer
<b>T<sub>r</sub></b>	: Reference Temperature
<b>E<sub>a</sub></b>	: Activation Energy
<b>KB</b>	: Boltzman Constant



## LIST OF TABLES

	<u>Page</u>
<b>Table 4.1</b> : Prepared Electrolyte Solutions.....	22
<b>Table 5.1</b> : Crystallite sizes of the synthesized cathode materials. ....	27
<b>Table 5.2</b> : Conductivity and activation energy values vs. carbon content.....	30
<b>Table 5.3</b> : Theoretical and actual carbon contents.....	32
<b>Table 5.4</b> : XPS information of chemically oxidized $\text{Li}_2\text{MnSiO}_4$ .....	39
<b>Table 5.5</b> : Carbon contents vs. highest observed capacities .....	44
<b>Table 5.6</b> : Capacity values of the batteries prepared using different electrolyte solutions .....	46
<b>Table 5.7</b> : XPS information of electrochemically oxidized $\text{Li}_2\text{MnSiO}_4$ .....	47



## LIST OF FIGURES

	<u>Page</u>
<b>Figure 2.1</b> : Graph of mass and volume energy densities of several secondary cells..	4
<b>Figure 2.2</b> : Li-ion secondary battery charge mechanism. ....	4
<b>Figure 2.3</b> : Diagram of the charging of a secondary cell battery.....	5
<b>Figure 3.1</b> : Diagram of TGA devices. ....	9
<b>Figure 3.2</b> : Diagram of XRD devices. ....	10
<b>Figure 3.3</b> : Diagram of an XPS system. ....	11
<b>Figure 3.4</b> : Diagram of a 4 point probe tester. ....	12
<b>Figure 3.5</b> : Diagram of a DSC device.....	13
<b>Figure 4.1</b> : Furnaces that are used for the $\text{Li}_2\text{MnSiO}_4$ production.....	16
<b>Figure 4.2</b> : A core – shell figure where core represents the $\text{Li}_2\text{MnSiO}_4$ crystallites and shell represents the oxidized layer. ....	16
<b>Figure 4.3</b> : Theoretical $\text{Li}_2\text{MnSiO}_4$ (Pmn2 <sub>1</sub> ) LSDA structure prepared by `Mercury` program. ....	19
<b>Figure 4.4</b> : Comparison of the theoretical XRD patterns. ....	19
<b>Figure 5.1</b> : XRD patterns of theoretical and synthesized $\text{Li}_2\text{MnSiO}_4$ and C/ $\text{Li}_2\text{MnSiO}_4$ samples. ....	27
<b>Figure 5.2</b> : Conductivity graphic of 10% C/ $\text{Li}_2\text{MnSiO}_4$ .....	28
<b>Figure 5.3</b> : Conductivity graphic of 15% C/ $\text{Li}_2\text{MnSiO}_4$ .....	28
<b>Figure 5.4</b> : Conductivity graphic of 20% C/ $\text{Li}_2\text{MnSiO}_4$ .....	29
<b>Figure 5.5</b> : Conductivity graphic of 25% C/ $\text{Li}_2\text{MnSiO}_4$ .....	29
<b>Figure 5.6</b> : Conductivity graphic of 30% C/ $\text{Li}_2\text{MnSiO}_4$ .....	30
<b>Figure 5.7</b> : TGA graphic of theoretically 10% C/ $\text{Li}_2\text{MnSiO}_4$ .....	31
<b>Figure 5.8</b> : TGA graphics of theoretically 15% (left) and 20% (right) C/ $\text{Li}_2\text{MnSiO}_4$ .....	31
<b>Figure 5.9</b> : TGA graphics of theoretically 25% (left) and 30% (right) C/ $\text{Li}_2\text{MnSiO}_4$ .....	32
<b>Figure 5.10</b> : XRD comparison graphic for the sample oxidized using $\text{H}_2\text{O}_2$ . ....	33
<b>Figure 5.11</b> : XRD comparison graphic for the sample oxidized using 1M $\text{K}_2\text{S}_2\text{O}_8$ .....	34
<b>Figure 5.12</b> : XRD comparison graphic for the sample delithiated using 5M $\text{K}_2\text{S}_2\text{O}_8$ .....	34
<b>Figure 5.13</b> : XRD comparison graphic for the sample oxidized using 1M $\text{H}_2\text{SO}_4$ . 35	35
<b>Figure 5.14</b> : XRD comparison graphic for the sample oxidized using 2M $\text{H}_2\text{SO}_4$ . 35	35
<b>Figure 5.15</b> : XRD comparison graphic for the sample oxidized by heat treatment for 30 minutes.....	36
<b>Figure 5.16</b> : XRD comparison graphic for the sample oxidized by heat treatment for 24 hours.....	36
<b>Figure 5.17</b> : XRD comparison graphic for the sample oxidized using $\text{NH}_3$ for 24 hours.....	37

<b>Figure 5.18</b> : XRD comparison graphic for the sample oxidized using NH <sub>3</sub> for 72 hours. ....	37
<b>Figure 5.19</b> : An example for the XPS graphics of oxidized Li <sub>2</sub> MnSiO <sub>4</sub> samples. ...	39
<b>Figure 5.20</b> : Comparison graphics of batteries containing 10% C/Li <sub>2</sub> MnSiO <sub>4</sub> and LiPF <sub>6</sub> (EC:DEC). ....	40
<b>Figure 5.21</b> : Comparison graphics of batteries containing 10% C/Li <sub>2</sub> MnSiO <sub>4</sub> and LiPF <sub>6</sub> (EC:DMC). ....	40
<b>Figure 5.22</b> : Comparison graphics of batteries containing 15% C/Li <sub>2</sub> MnSiO <sub>4</sub> and LiPF <sub>6</sub> (EC:DEC). ....	41
<b>Figure 5.23</b> : Comparison graphics of batteries containing 15% C/Li <sub>2</sub> MnSiO <sub>4</sub> and LiPF <sub>6</sub> (EC:DMC). ....	41
<b>Figure 5.24</b> : Comparison graphics of batteries containing 20% C/Li <sub>2</sub> MnSiO <sub>4</sub> and LiPF <sub>6</sub> (EC:DEC). ....	42
<b>Figure 5.25</b> : Comparison graphics of batteries containing 20% C/Li <sub>2</sub> MnSiO <sub>4</sub> and LiPF <sub>6</sub> (EC:DMC). ....	42
<b>Figure 5.26</b> : Comparison graphics of batteries containing 25% C/Li <sub>2</sub> MnSiO <sub>4</sub> and LiPF <sub>6</sub> (EC:DEC). ....	43
<b>Figure 5.27</b> : Comparison graphics of batteries containing 25% C/Li <sub>2</sub> MnSiO <sub>4</sub> and LiPF <sub>6</sub> (EC:DMC). ....	43
<b>Figure 5.28</b> : Comparison graphics of batteries containing 30% C/Li <sub>2</sub> MnSiO <sub>4</sub> and LiPF <sub>6</sub> (EC:DEC). ....	44
<b>Figure 5.29</b> : Figure 5.29. Comparison graphics of batteries containing 30% C/Li <sub>2</sub> MnSiO <sub>4</sub> and LiPF <sub>6</sub> (EC:DMC). ....	44
<b>Figure 5.30</b> : An example for the batteries prepared using 30% C/Li <sub>2</sub> MnSiO <sub>4</sub> cathode material and an electrolyte solution containing LiTFSI salt. ....	45
<b>Figure 5.31</b> : Comparison graphics of batteries containing 30% CCL Li <sub>2</sub> MnSiO <sub>4</sub> and LiClO <sub>4</sub> (EC:DEC). ....	46
<b>Figure 5.32</b> : DSC comparison of the electrolyte solutions. ....	48
<b>Figure 5.33</b> : Degradation graphic of the most stable electrolyte solution. ....	48

## SUMMARY

### CHEMICAL DEINTERCALATION AND STABILITY INVESTIGATION OF NANOSIZED C/Li<sub>2</sub>MnSiO<sub>4</sub> CATHODE MATERIAL WITH DIFFERENT ELECTROLYTES

Rechargeable lithium ion (Li-ion) batteries are commercially used for portable electronics and light electrical devices since 1991. Despite of the wide variety of applications, most commonly used Li-ion batteries have important problems related to their safety, environmental impact and high cost of materials. Thus, a research interest in production of alternative cathode materials have arisen, where dilithium orthosilicates (Li<sub>2</sub>MSiO<sub>4</sub>, M = Co, Ni, Mn, Fe) are mostly preferred for being safe, environmentally friendly, cheaper and thermally and chemically stable. Besides these, Li<sub>2</sub>MSiO<sub>4</sub> have a very important advantage of theoretical possibility for reversible exchange of up to two lithium ions per formula unit that leads to high capacities up to 333 mAh/g.

In this study, Li<sub>2</sub>MnSiO<sub>4</sub> nanoparticles were synthesized via sol-gel Pechini type synthesis and coated with different amounts of conductive carbon layer (10, 15, 20, 25 and 30 wt.%) by water mediated impregnation process to improve the electrical conductivity. Afterwards, R2032 coin-cell type batteries were assembled by using C/Li<sub>2</sub>MnSiO<sub>4</sub> nanocomposites as cathode material and 9 different electrolytes. Besides these, pristine Li<sub>2</sub>MnSiO<sub>4</sub> materials were tried to be chemically delithated by using different oxidizing agents in order to observe if delithiation of both lithium atoms is possible.

XRD was used to observe structure of the synthesized and modified samples while TGA was used to determine the actual carbon content in composite materials. XPS was used to determine oxidation state of Mn in both chemically and electrochemically delithated samples. DSC was used to examine the reactivity of pristine sample with electrolyte solutions and EC measurements were done to compare the effect of carbon coating loading on conductivity of the cathode materials. Finally, galvanostatic charge-discharge tests were performed to observe electrochemical performance and practical capacities of prepared materials.

It was observed from the XRD results that, nanosized Li<sub>2</sub>MnSiO<sub>4</sub> particles are successfully synthesized and the structure of the material was maintained after water mediated impregnation processes. TGA measurements showed that the water mediated impregnation process is accurate to coat Li<sub>2</sub>MnSiO<sub>4</sub> with the desired amount of carbon.

Studies proved that applied technique was successful for the synthesis of pristine Li<sub>2</sub>MnSiO<sub>4</sub> nanoparticles having Pmn2<sub>1</sub> configuration in the range of 35 – 50 nm. It is also seen that amount of carbon loading could be precisely controlled during synthesis of C/Li<sub>2</sub>MnSiO<sub>4</sub> nanocomposites using water impregnation process.

According to the conductivity measurements, electrical conductivity of the C/Li<sub>2</sub>MnSiO<sub>4</sub> nanopowders could be increased by optimizing, in this case increasing, the carbon loading in the composites. It is seen that formation reaction of a passivation layer affects the measured cell capacity during the first cycle of galvanostatic charge-discharge tests. Thus, capacity values measured for the second charge-discharge cycles are used to compare the battery capacities. Even though highest stability (least reactivity) is observed for LiClO<sub>4</sub>(TMS:EMC) between the studied electrolyte solutions; highest battery capacity, based on the charge discharge tests, is observed for the organic electrolytes containing LiPF<sub>6</sub> salts. The highest battery capacity observed throughout the study was 177.0 mAh/g, for the second charge-discharge cycle, and it was measured for the battery prepared using C/Li<sub>2</sub>MnSiO<sub>4</sub> nanocomposite containing 30 wt.% of carbon and 1M LiPF<sub>6</sub> in EC:DMC electrolyte solution. XPS analyses of the C/Li<sub>2</sub>MnSiO<sub>4</sub> nanocomposite, taken out of the same type of battery after charging process, showed that complete delithiation of the cathode materials could be done electrochemically. Neither of the applied chemical delithiation techniques were successful for complete delithiation of the pristine samples, among which only 3 of them could chemically delithiated pristine Li<sub>2</sub>MnSiO<sub>4</sub> nanoparticles.

## ÖZET

### **C/Li<sub>2</sub>MnSiO<sub>4</sub> KATOT MALZEMESİNİN KİMYASAL DEİTERKALASYONU VE FARKLI ELEKTROLİTLER İLE KARARLILIĞININ İNCELENMESİ**

Taşınabilir elektronik eşyalar ve hafif elektrikli cihazlarda kullanılan şarj edilebilir lityum iyon (Li-iyon) pilleri 1991 yılından beri ticari olarak üretilmekte ve yaygın bir şekilde kullanılmaktadır. Çok çeşitli uygulama alanlarına sahip olmalarına rağmen; lityum iyon pillerinin kullanımında güvenlik, çevreye olan etkileri ve kullanılan malzemelerin yüksek fiyatlı olması gibi önemli sorunlar söz konusudur. Bu sebeple alternatif elektrot malzemelerinin üretimi pek çok araştırmacının ilgisini çeken bir konu haline gelmiştir. Günümüzde yaygın olarak mono-lityum elektrot malzemeleri kullanılsa da, alternatif katot ve anot malzemelerinin üretiminde özellikle di-lityum ortosilikat (Li<sub>2</sub>MSiO<sub>4</sub>, M = Co, Ni, Mn, Fe) temelli malzemeler gelecek vadetmektedir. Di-lityum ortosilikatların tercih edilmelerinin başlıca nedenleri daha güvenli, çevre dostu, kullanılan diğer elektrot malzemelerinin çoğuna göre daha ucuz ve hem termal hem de kimyasal olarak daha kararlı olmalarıdır. Bu özelliklerinin yanı sıra di-lityum ortosilikatların çok önemli bir avantajı da, teorik olarak, di-lityum ortosilikatların birim yapılarındaki her iki lityum atomunun da geri dönüşebilir bir şekilde reaksiyona katılabilme olasılığıdır. Di-lityum ortosilikatların birim yapılarındaki iki lityum atomunun da geri dönüşebilir bir şekilde reaksiyona katılabilme olasılığının getirdiği avantaj ise, teoride, bu malzemelerin kullanıldığı pillerin kapasitelerinin 333 mAh/g'a kadar çıkabilme potansiyeli olduğunu göstermesidir.

Sol-gel yöntemi; 'jel' (gel) adı verilen, ayrık parçacıkların veya ağı polimerlerin (polymer networks) oluşturduğu, entegre ağı oluşumu için prekürsör görevi görmek amacıyla monomerlerin 'sol' adı verilen kolloidal çözeltilere dönüşmesi sürecidir ve bu çalışmada, Li<sub>2</sub>MnSiO<sub>4</sub> nanoparçacıkları Pechini tipi sol-gel yöntemiyle sentezlenmiştir. Prekürsör sentezi için başlangıç bileşenleri olarak lityum asetat dehidrat, mangan asetat tetrahidrat, etilen glikol, sitrik asit, etanol ve tetraetoksisilan kullanılmıştır. Başlangıç bileşenlerinin molariteleri, uygun sitokiyometrik oranı sağlamak amacıyla, 1:1:18:6:4:16 - Mn:Si:C<sub>2</sub>H<sub>6</sub>O<sub>2</sub>:C<sub>6</sub>H<sub>8</sub>O<sub>7</sub>:C<sub>2</sub>H<sub>5</sub>OH:H<sub>2</sub>O olarak belirlenmiştir. Tek fazlı bir ürün elde edilebilmesi için lityum asetatın, belirlenen sitokiyometrik orana göre, kütlece (wt.%) 20% fazlası reaksiyona sokulmuştur. Başlangıç bileşenlerinin bir gaz reaktörü içinde çözünme süreci boyunca ortamda sabit bir argon akışı (akış hızı: 5,7 l/saat) sağlanmıştır. Öncelikle metal asetatların tamamen çözünmesi için çözücü (su) 35°C'ye ısıtılmış daha sonra da elde edilen karışım 60°C'ye ısıtılıp etilen glikol, tetraetil ortosilikat (TEOS) ve birkaç damla konsantre hidroklorik asit eklenerek metal sitratların polimerizasyonu başlatılmıştır. Reaksiyon 24 saat boyunca kapalı bir reaktörde sürdürüldükten sonra elde edilen jel, öncelikle 60°C sıcaklıkta kapalı bir reaktörde argon atmosferi altında 3 gün boyunca bekletilmiş daha sonra da yine 60°C sıcaklıkta bir etüvde 3 gün boyunca

dinlendirilmiştir. Elde edilen prekürsör jel, argon atmosferinde, altın bir kroze içinde 12 saat boyunca kalsine edilerek prekürsörün organik matrisi termal olarak ayrıştırılmıştır (decomposition). Kalsinasyon işlemi boyunca argon akışı sabit (akış hızı: 30 ml/dakika) tutulmuş ve fırın içi sıcaklığı 800°C'ye ulaştıktan sonra (ısınma hızı: 5°C/dakika) on iki saatlik süre başlatılmıştır. Kalsinasyon işleminden sonra, ortamdaki dekompoze olmuş organik matrisin giderilmesi için, elde edilen malzeme ball milling işlemi ile öğütülüp toz haline getirildikten sonra yine altın bir kroze içinde ve sabit hava akışı (akış hızı: 150 ml/dakika) altında 800°C'de 6 saat boyunca bekletilmiştir. İkinci aşamaya benzer olarak ısınma hızı 5°C/dakika olarak ayarlanmış ve altı saatlik reaksiyon süresi fırın 600°C'ye ulaştıktan sonra başlatılmıştır. Fırındaki hava akışı sebebiyle üçüncü aşama sonrasında elde edilen  $\text{Li}_2\text{MnSiO}_4$  nanoparçacıkları kısmi olarak okside olduğundan, saf  $\text{Li}_2\text{MnSiO}_4$  nanoparçacıklarının elde edilebilmesi için, okside olmuş dış kabuk bir indirgeme reaksiyonu ile giderilmiştir. Saf  $\text{Li}_2\text{MnSiO}_4$  nanoparçacıklarının elde edilebilmesi için uygulanan son aşama olan bu dördüncü aşamada, kısmen okside olmuş  $\text{Li}_2\text{MnSiO}_4$  nanoparçacıkları öğütülüp toz haline getirildikten sonra ince kuvars bir borunun ortasına kuvars fiberler kullanılarak sabitlenmiş ve argon atmosferi altında 600°C'ye ısıtılmıştır (ısınma hızı: 10°C/dakika). Bu süreçte ve fırın 600°C'ye ulaştıktan sonraki 1 saatlik reaksiyon süresi boyunca fırın içinde sabit bir hızda hidrojen ve argon akışı ( $\text{H}_2:\text{Ar} = 1:9$ , akış hızı: 50ml/dakika.) sağlanmıştır.

Çalışmada, saf  $\text{Li}_2\text{MnSiO}_4$  nanoparçacıklarının yanı sıra, farklı oranlarda iletken karbon tabakası ile kaplı  $\text{C}/\text{Li}_2\text{MnSiO}_4$  nanokompozitler de sentezlenmiştir.  $\text{C}/\text{Li}_2\text{MnSiO}_4$  nanokompozitlerinin sentezlenmesinde, pilin şarj ve deşarj aşamalarında pil kapasitesinin azalmasına sebep olan hacim bozunumu (volume distortion) gibi etkenlerin eliminasyonu ve katot malzemesinin elektriksel iletkenliğinin artırılması hedeflenmiştir. Bu işlem için, saf  $\text{Li}_2\text{MnSiO}_4$  nanoparçacıklarının sentezinde izlenen yol üçüncü aşamanın sonuna kadar aynen tekrarlanmıştır. Saf  $\text{Li}_2\text{MnSiO}_4$  nanoparçacık sentezinden farklı olarak, üçüncü aşamadan sonra elde edilen kısmen oksitlenmiş  $\text{Li}_2\text{MnSiO}_4$  nanoparçacıkları indirgeme reaksiyonuna sokulmayıp bunun yerine farklı miktarlarda iletken karbon tabakaları ile kaplanmıştır.  $\text{C}/\text{Li}_2\text{MnSiO}_4$  nanokompozitlerinin sentezinde su aracılıklı doyurma (water mediated impregnation) yöntemi kullanılmıştır ve  $\text{C}/\text{Li}_2\text{MnSiO}_4$  nanokompozitlerinin içerdiği karbon miktarının etkilerinin gözlenmesi amacıyla kaplanan karbon miktarı kütlece (wt.%) 10%, 15%, 20%, 25% ve 30% olarak belirlenmiştir. Su aracılıklı doyurma işleminde, öğütülüp toz haline getirilmiş kısmen oksitlenmiş  $\text{Li}_2\text{MnSiO}_4$  nanoparçacıklar yarım küre şeklindeki elastik kaplarda piromellitik asitin (PMA) sulu çözeltileri ve Poli-N-vinilformamid (PNVF) ile karıştırılıp ısıtılmıştır. Isıtma işlemi çözeltideki tüm su buharlaşıp çözelti kahverengi çamurumsu bir hal alana kadar devam etmiştir. Sıcaklık 50°C'den sonra kademeli olarak artırılıp, kaynamayı önlemek amacıyla, işlem süresince 100°C'nin altında tutulmuş ve karışım bir manyetik karıştırıcı yardımıyla işlem süresince orta hızda karıştırılmıştır. Poli-N-vinilformamid'in (PNVF) yalnızca kütlece beşte biri (20 wt.%) karbon kaynağı olarak kullanılabilirdiğinden, Poli-N-vinilformamid (PNVF) miktarı kaplanmak istenen  $\text{Li}_2\text{MnSiO}_4$  nanoparçacıklarının miktarının beş katı olarak alınmıştır. Piromellitik asit (PMA) miktarı ise, kullanılan Poli-N-vinilformamid (PNVF) miktarının kütlece yüzde beşi (5 wt.%) olarak belirlenmiştir. Su aracılıklı doyurma işlemi, karışımın içerdiği su miktarıyla orantılı olarak, 4-6 saat arası sürmüştür. Su miktarı, çökeltme (sedimentation) ve tanecik kümelenmesine (grain agglomeration) müsaade etmeyecek kadar azalıp çamurumsu bir karışım elde

edildikten sonra elde edilen karışımlar 90°C'lik bir etüvde 24 saat boyunca dinlendirilmiştir. Etüvdeki 24 saatlik dinlenme aşamasından sonra elde edilen malzeme öğütülüp toz haline getirilerek, farklı miktarlarda karbon içeren, C/Li<sub>2</sub>MnSiO<sub>4</sub> nanokompozitleri elde edilmiştir.

Sentezlenen tüm malzemeler için X-ışını kırınımı (X-ray Diffraction, XRD) analizleri kullanılarak saf (pristine) Li<sub>2</sub>MnSiO<sub>4</sub> nanoparçacıklarının ve C/Li<sub>2</sub>MnSiO<sub>4</sub> nanokompozitlerinin başarılı bir şekilde sentezlenip sentezlenmediği incelenmiş ve ortalama tanecik boyutu hesaplanmıştır. XRD analizlerine ek olarak, C/Li<sub>2</sub>MnSiO<sub>4</sub> nanokompozitlerindeki karbon miktarının belirlenmesi için termo-gravimetrik analizler (TGA) yapılmıştır. Bu analizlerin ışığında, su aracılıklı doyurma işleminin, Li<sub>2</sub>MnSiO<sub>4</sub> nanoparçacıklarını istenilen miktarda karbon ile kaplamakta başarılı olup olmadığı ve işlemin Li<sub>2</sub>MnSiO<sub>4</sub> yapısı üzerindeki etkileri incelenmiştir. Çalışmada, Lityum hekzaflorofosfat (LiPF<sub>6</sub>), lityum perklorat (LiClO<sub>4</sub>), lityum bis(okzalato)borat (LiBOB) ve lityum bis(triflorometanosülfonil)imid (LiTFSI) tuzları ile etilen karbonat (EC) etil metil karbonat (EMC), dimetil karbonat (DMC), dietil karbonat (DEC) ve 1,1-dioksit tetrametilen sülfon (TMS) çözücüleri kullanılarak 12 farklı elektrolit çözeltisi hazırlanmıştır. Deneylerde, LiTFSI tuzu içeren çözeltilerdeki çözünme problemi sebebiyle, yalnızca LiPF<sub>6</sub>(EC:DEC), LiPF<sub>6</sub>(EC:DMC), LiPF<sub>6</sub>(TMS:EMC), LiClO<sub>4</sub>(EC:DEC), LiClO<sub>4</sub>(EC:DMC), LiClO<sub>4</sub>(TMS:EMC), LiTFSI(EC:DEC), LiTFSI(EC:DMC) ve LiTFSI(TMS:EMC) organik elektrolitleri kullanılmıştır.

Çalışmada kullanılacak elektrolit çözeltilerinin argon ve hava atmosferi altındaki bozunumunun incelenmesi amacıyla tüm çözeltiler diferansiyel taramalı kalorimetri (DSC) testleri ile analiz edilmiştir. Buna ek olarak, elektrolit çözeltilerinin sentezlenen saf Li<sub>2</sub>MnSiO<sub>4</sub> nanoparçacıklarına karşı kararlılıkları da diferansiyel taramalı kalorimetri (DSC) analizleri ile incelenerek en az reaktif elektrolit çözeltileri tespit edilmiştir. Diferansiyel taramalı kalorimetri (DSC) analizlerinde argon (akış hızı: 80 ml/min.) ve hava akışı sabit tutulup; sıcaklık, dakikada 10°C artırılmak suretiyle, 25°C'den 400°C'ye çıkartılmıştır.

X-ışını kırınımı (XRD) ve termogravimetrik analizlerden (TGA) sonra AC (33 Hz) 4-probe tekniği kullanılarak sentezlenmiş olan; kütlece 10%, 15%, 20%, 25% ve 30% karbon içeren, toz halindeki C/Li<sub>2</sub>MnSiO<sub>4</sub> nanokompozit katot malzemelerinin elektriksel iletkenlikleri hesaplanmış ve karşılaştırılmıştır. Karşılaştırmalar sonucunda nanokompozitlerdeki karbon miktarının elektriksel iletkenlik üzerindeki etkileri incelenmiştir.

X-ışını kırınımı analizleri, termogravimetrik analizler ve iletkenlik ölçümlerinden sonra farklı miktarlarda karbon içeren nanokompozit katot malzemeleri ile farklı elektrolit çözeltileri kullanılarak R2032 coin tipi piller hazırlanmış ve galvanostatik şarj-deşarj testleri ile pil performansları incelenmiştir.

Galvanostatik şarj-deşarj testlerinin birinci setinde, kütlece 15% karbon içeren ve alüminyum film üzerine kaplanmış, C/Li<sub>2</sub>MnSiO<sub>4</sub> nanokompozit katot malzemesi (15C/Li<sub>2</sub>MnSiO<sub>4</sub>) ve 9 farklı elektrolit çözeltisi kullanılarak 9 çeşit R2032 coin tipi pil yarı hücresi hazırlanmıştır. Yapılan şarjdeşarj testleri sonucunda en yüksek kapasitenin ölçüldüğü pillerde kullanılmış olan 2 adet elektrolit çözeltisi 2. aşama şarj-deşarj testlerinde kullanılmak üzere belirlenmiştir.

Galvanostatik şarj-deşarj testlerinin ikinci setinde, kütlece 10%, 15%, 20%, 25% ve 30% karbon içeren toz halindeki C/Li<sub>2</sub>MnSiO<sub>4</sub> nanokompozit katot malzemeleri ile

LiPF<sub>6</sub>(EC:DEC) ve LiPF<sub>6</sub>(EC:DMC) elektrolit çözeltileri kullanılarak 10 çeşit R2032 coin tipi pil yarı hücresi hazırlanmıştır. Testler sonucunda elde edilen pil kapasitesi değerleri kullanılarak, hazırlanan piller arasında en yüksek performansı gösteren pildeki nanokompozit katot malzemesinin içerdiği karbon miktarı tespit edilmiş ve bu malzeme 3. aşama şarj-deşarj testlerinde kullanılmıştır.

Galvanostatik şarj-deşarj testlerinin üçüncü setinde, kütlece 30% karbon içeren (30C/Li<sub>2</sub>MnSiO<sub>4</sub>) toz halindeki C/Li<sub>2</sub>MnSiO<sub>4</sub> nanokompozit katot malzemeleri ile 9 farklı elektrolit çözeltisi kullanılarak 9 çeşit R2032 coin tipi pil yarı hücresi hazırlanmıştır. Şarjdeşarj testleri hazırlanan 9 çeşit pil yarı hücresi için uygulanmış ve pillerin kapasitesi karşılaştırılmıştır. En yüksek performansı gösteren pil yarı hücresi çeşidi tekrar hazırlanıp tamamen şarj edildikten sonra, 30C/Li<sub>2</sub>MnSiO<sub>4</sub> nanokompozit katot malzemesi pilden çıkartılmış ve manganın yükseltgenme basamağı X-ışını fotoelektron spektroskopisi (XPS) ile ölçülmüştür. Yapılan ölçümde, pildeki katot malzemesinin yapısında bulunan lityum iyonlarının elektrokimyasal olarak birim hücreden ayrılıp ayrılmadığı (delithiation) ve lityum iyonlarının pil reaksiyonlarına katılma oranı gözlemlenmiştir.

Elektrokimyasal delitiasyon (delithiation) testlerinin sonuçlarını desteklemek amacıyla, kimyasal delitiasyon testleri yapılmıştır. Saf katot malzemesi, lityum iyonlarını kimyasal yöntemlerle birim hücreden ayırmanın (delithiation) mümkün olup olmadığını görmek amacıyla hidrojen peroksit (H<sub>2</sub>O<sub>2</sub>), potasyum persülfat (K<sub>2</sub>S<sub>2</sub>O<sub>8</sub>), sülfürik asit (H<sub>2</sub>SO<sub>4</sub>) ve amonyak (NH<sub>3</sub>) ile yedi farklı deney düzeneğinde reaksiyona sokulmuştur. İlk deney setinde saf Li<sub>2</sub>MnSiO<sub>4</sub> nanoparçacıkları, asetik asit (CH<sub>3</sub>COOH) kullanılarak oluşturulmuş sulu asidik ortamda hidrojen peroksit (H<sub>2</sub>O<sub>2</sub>) ile 24 saat boyunca reaksiyona sokulmuştur. İkinci ve üçüncü deney setlerinde saf Li<sub>2</sub>MnSiO<sub>4</sub> nanoparçacıkları, asetik asit (CH<sub>3</sub>COOH) kullanılarak oluşturulmuş sulu asidik ortamda, sırasıyla 1M ve 2M potasyum persülfat (K<sub>2</sub>S<sub>2</sub>O<sub>8</sub>) ile 24 saat boyunca reaksiyona sokulmuştur. Dördüncü deney setinde kısmi oksidasyon hedeflendiği için saf Li<sub>2</sub>MnSiO<sub>4</sub> nanoparçacıkları 1M sülfürik asit ile (H<sub>2</sub>SO<sub>4</sub>) sulu asidik ortamda 24 saat boyunca reaksiyona sokulmuş ve beşinci sette aynı işlem 2M sülfürik asit ile tekrarlanmıştır. Altıncı ve yedinci deney setlerinde amonyak kullanılarak pH 12 olacak şekilde ayarlanmış ve saf Li<sub>2</sub>MnSiO<sub>4</sub> nanoparçacıkları bazik ortamda sırasıyla 24 ve 72 saat boyunca bekletilmiştir. Son olarak da saf Li<sub>2</sub>MnSiO<sub>4</sub> nanoparçacıkları kademeli olarak ısıtılıp 110 °C'lik yağ banyosunda 24 saat boyunca bekletilerek termal oksidasyon denenmiştir. Tüm bu reaksiyonların sonunda elde edilen materyaller santrifüjlenmiş ve 24 saat boyunca 90°C'lik etüvde kurutulduktan sonra X-ışını kırınımı analizleri yapılmıştır. XRD analizleri sonucunda LiMnSiO<sub>4</sub> ve MnSiO<sub>4</sub>'e benzeyen malzemeler için XPS analizleri yapılarak Li<sub>2</sub>MnSiO<sub>4</sub> nanoparçacıklarındaki manganın yükseltgenme seviyesi tespit edilmiştir.

Çalışmalar sonucunda, Pechini tipi sol-gel yöntemi kullanılarak Pmn<sub>2</sub> konfigürasyonuna sahip, 35-50 nm boyutlarında, saf Li<sub>2</sub>MnSiO<sub>4</sub> nanoparçacıklarının başarılı bir şekilde sentezlendiği XRD analizleri ile kanıtlanmıştır. Yine XRD analizlerinden yararlanılarak, su aracılıklı doyurma işlemi ile saf Li<sub>2</sub>MnSiO<sub>4</sub> nanoparçacıklarının yapılarını bozmadan, parçacıkların istenilen oranda karbon ile kaplanabildiği ve C/Li<sub>2</sub>MnSiO<sub>4</sub> nanokompozit katot malzemelerinin başarılı bir şekilde sentezlendiği gözlemlenmiştir. Farklı miktarlarda karbon içeren C/Li<sub>2</sub>MnSiO<sub>4</sub> nanokompozitlerinin iletkenlik ölçümleri ve galvanostatik şarjdeşarj testleri sonucunda, elektriksel iletkenliğin kompozitlerdeki karbon miktarının

artmasıyla arttığı ve pil kapasitelerinin katot malzemesinin karbon miktarıyla orantılı olarak arttığı kanıtlanmıştır. Diferansiyel taramalı kalorimetri testlerinde en yüksek kararlılık ve en düşük reaktivite  $\text{LiClO}_4$  içeren elektrolit çözeltileri için gözlenmiş olmakla birlikte, hazırlanan pillerin galvanostatik şarj deşarj analizleri sonucunda en yüksek kapasite  $\text{LiPF}_6$  tuzu içeren elektrolit çözeltileri ile hazırlanmış piller için gözlemlenmiştir. İlk şarj-deşarj döngüsünde pil kapasitesinin, pasivasyon tabakasını oluşturan reaksiyonlardan etkilendiği gözlemlendiği için hazırlanan pillerin kapasiteleri ikinci şarj-deşarj döngüleri baz alınarak karşılaştırılmıştır. Bu karşılaştırmaya göre, 2. şarj-deşarj döngüsünde, en yüksek kapasite  $177.0 \text{ mAh/g}$  olarak kütlece %30 karbon içeren  $\text{C/Li}_2\text{MnSiO}_4$  nanokompozit katot malzemesi ve  $1\text{M LiPF}_6(\text{EC:DMC})$  elektrolit çözeltisi içeren pil için ölçülmüştür. Aynı pil kombinasyonu tamamen şarj edildikten sonra, kullanılan nanokompozit katot malzemesindeki manganın yükseltgenme basamağı XPS analizleri ile  $3.8$  olarak ölçülmüştür. Bu sonuca dayanılarak,  $\text{C/Li}_2\text{MnSiO}_4$  nanokompozit katot malzemesinin elektrokimyasal delitiasyonunun yapılabildiği gözlemlenmiştir. Kimyasal delitiasyon ise, saf  $\text{Li}_2\text{MnSiO}_4$  nanoparçacıkları için, uygulanan yöntemlerin yalnızca üçünde kısmi olarak sağlanabilmiştir.



## 1 . INTRODUCTION

Energy storage devices composed from electrochemical cells, or more commonly called batteries, have a long history. Despite of the ancient discovery called `Baghdad Battery` produced BC, studies of Luigi Galvani and Alessandro Volta at the end of the eighteenth century are attributed as the first examples of direct production of electricity from chemical reactions [1, 2]. A lot of electrochemical systems have been developed in the nineteenth century on the basis of Volta`s work, in which Georges-Lionel Leclanche`s cell concept is still used for the consumer (carbon-zinc and alkaline) primary batteries. First example of the secondary/rechargeable batteries was the lead-acid battery produced by Gaston Plante in 1859 which was followed by the nickel-cadmium battery produced by Waldmar Jungner in 1901. Along with several modifications such as packaging and construction design, battery system produced by Waldmar Jungner is still the base of the popular commercial batteries of nowadays such as batteries used for car ignition and portable tools. Even though battery prototypes produced by Leclanche, Plante and Junger were sufficient enough for a long time, dramatic increase in the demand of portable energy created a research interest in the alternative battery production in the late 1960`s. Researches were mainly focused on increasing the energy density and operation time while decreasing the production costs.

With the usage of lithium metal as the electrode material in 1970`s, energy density value is drastically increased according to traditional systems like nickel-cadmium and nickel metal hydride batteries [3]. But important problems related to their safety, environmental impact and high cost of materials also came along with this advantage. Thus, many modifications like using manganese dioxide as the cathode material had to be applied for the further improvement of the lithium ion battery properties. Even though all of the initial lithium batteries used for the consumer electronics (such as electronic watches, toys and cameras) were primary batteries; secondary batteries gained an importance with the invention of the insertion/intercalation electrodes in 1978 [2]. Basic principle of the rechargeable lithium batteries were dependent on compounds having open structures which can

reversibly accept and release lithium ions in and out during the charging – discharging processes. It was necessary to balance the positive charge of the inserted lithium ion while preventing collapse of the crystal structure in order to provide continuous electrochemical reactions. And, these requirements could be obtained by using the transition metals in the electrode materials.

Today, lithium batteries are used for many popular consumer products such as mobile phones, laptops, camcorders, Mp3s and light electrical vehicles. But, energy density of the currently used Li batteries are still not high enough to replace the devices like internal combustion cars, using oil resources, with environmentally friendly controlled emission cars; such as hybrid vehicles (HEVs) and electric vehicles (EV).

Since, fossil fuel reserves are continuously decreasing while level of the environmental pollution is dramatically increasing, renewable and green energy production became a very important need for the humanity. Unfortunately, despite of the valuable benefits of renewable energies such as solar and wind energies, their application fields have many limitations. Thus, improvement of the lithium ion batteries can play a very important role for the production of more environmentally benign devices

## **2 . BATTERIES**

Batteries are energy storage devices that can store electrical energy in the form of chemicals and make it possible to re-convert those chemicals into direct-current electricity [4]. They have gained an important place in our daily lives in the last few decades, especially with the wide usage of mobile phones and laptops, and as a result a research interest in development of new type of batteries have arisen [5].

Batteries can be classified in two main groups as primary and secondary batteries/cells where primary cell represents the non-rechargeable energy storage devices while secondary cell represents the rechargeable ones. Operation principle is similar for most of the secondary batteries. They are consist of voltaic cells, which are consist of two half-cells connected in series by a conductive electrolyte solution. During charging process, cations are reduced at the cathode with the electron addition and during discharging process, anions are oxidized because of the electron removal. Energy production in batteries undergoes by redox reactions on both electrodes, while discharging process, in the voltaic cells with the cation migration form the negative electrode (anode) to the positive electrode (cathode). Along with the electrodes, electrolyte solutions also have an important role in the batteries to provide ions flow. Because in order to provide ionic current flow, ions should be transferred between electrodes even though electrodes are not directly in electrical contact. Thus, both advancing the electrodes and advancing the electrolyte solutions are important research topics for the energy industry [4, 6, 7].

### **2.1 Rechargeable Batteries**

Rechargeable batteries, also known as the secondary batteries, mainly differ from the primary batteries with their ability to provide electrically reversible electrochemical reactions. Different types of secondary batteries having different capacities exist and they can be produced in different shapes and sizes (Figure 2.1.).

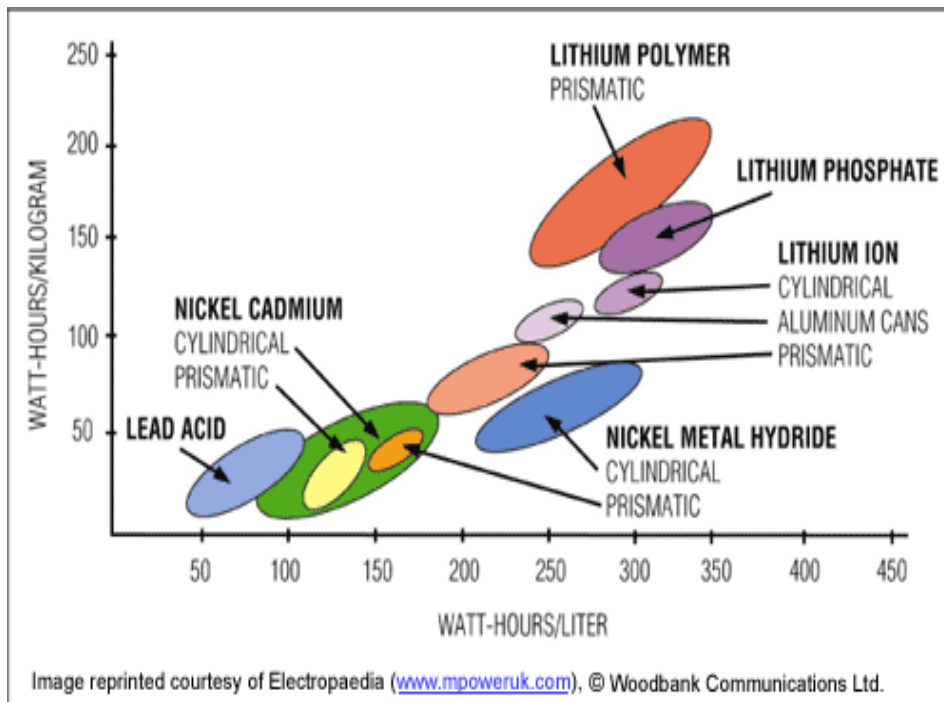


**Figure 2.1.** Graph of mass and volume energy densities of several secondary cells.

Other important differences of secondary batteries, from the primary batteries, can be indicated as lower total cost of use and lower level of environmental pollution related to the fewer amount of disposal. As a consequence, rechargeable batteries are preferred for production of the most commonly used industrial applications such as portable consumer devices and light vehicles (laptops, mobile phones, wheelchairs, golf carts, electric bicycles etc.).

Working principle of the rechargeable batteries can be explained with redox reactions. Electrons that are produced from oxidation of the positive active material, move through the electrolyte solution and be consumed by the negative material in order to reduce it during charging process (Figure 2.2.).

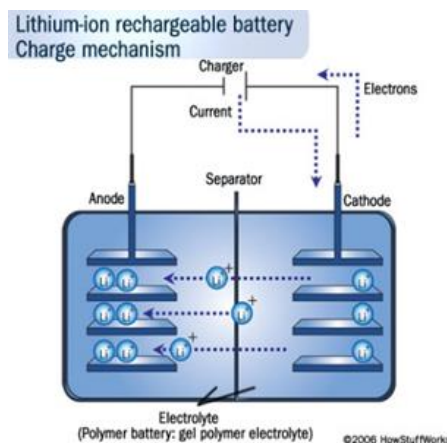


**Figure 2.2.** Li-ion secondary battery charge mechanism.

Similarly during the discharging process, material which was oxidized while charging is reduced and material which was reduced while charging is oxidized. Thus a current flow can be generated in the external circuit related to the electron movement during both processes (Figure 2.3.). In cases like lead-acid cells, electrolyte is an active reactant for the electrochemical reaction unlike the lithium-ion and nickel-cadmium cells in which it only serves as a simple buffer for the internal ion flow.

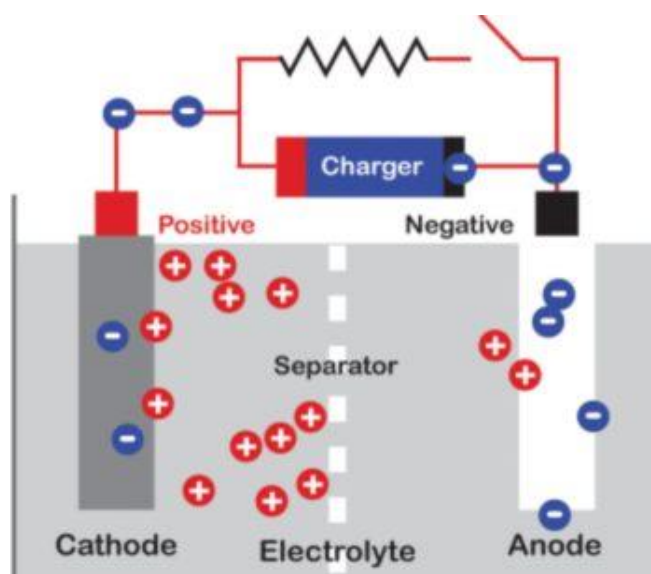


**Figure 2.3.** Diagram of the charging of a secondary cell battery.

It is possible to produce secondary batteries with many different chemicals but lead acid (LA), nickel metal hydride (NiMH), nickel cadmium (NiCd), lithium ion (Li-ion) and lithium ion polymer (Li-ion polymer) are the most commonly used technologies for rechargeable batteries.

### 2.1.1 Lithium ion batteries

As mentioned in the previous paragraph, lithium ion (Li-ion) batteries are one of the most preferred rechargeable battery types for many industrial applications. Despite of their high costs, Li-ion batteries dominate the consumer electronics market for being approximately 35% less heavy and resistant against the memory effect. Furthermore, their advantages like having better stability, longer cycle life, high power and high energy densities are also equally important for the Li-ion batteries [4, 10]. Major problem of the Li-ion batteries is safety concerns related to their high reactivity

towards water and air. Even though being unstable with respect to aqueous electrolytes and many organic liquids can be limiting for lithium usage in large-scale industrial applications, reasonable electrical conductivities can be obtained by using non-aqueous electrolytes. Proper non-aqueous electrolytes for Li batteries can be classified in five categories as conductive polymers, conductive ceramics, fused Li salts, solutions of Li salts in polar organic liquids and solutions of Li salts in polar inorganic liquids. Solutions of Li salts in polar organic liquids are especially important for their ability to form a passivation layer on the surface of Li metal which inhibits further decomposition in case of being exposed to air [4].

Even though Li-ion batteries can be produced with different shapes such as cylindrical, square or rectangular; their components and working principles are similar. A separator which is wetted using an electrolyte solutions is pressed between thin layers of a positive and a negative electrode in order to maintain a current flow in the cells. Micro pores on the separator allows ions to pass through while preventing direct connection of the positive and negative electrodes. In the studies, positive electrode is made of the conductive carbon layer coated lithium manganese silicate (C/Li<sub>2</sub>MnSiO<sub>4</sub>) and negative electrode is made of the metallic lithium. When the battery charges, ions of lithium move through the electrolyte from the positive electrode to the negative electrode and attach to the metallic lithium. And during discharge, lithium ions move back to the Li<sub>2</sub>MnSiO<sub>4</sub> from the metallic lithium [11].

### **2.1.2 Cathode materials**

Cathode materials are an indispensable part of all batteries that can be classified in two categories. First type of cathode materials can be defined as layered compounds having anion close-packed lattices such as LiTiS<sub>2</sub>, LiCoO<sub>2</sub>, LiNi<sub>1-x</sub>Co<sub>x</sub>O<sub>2</sub> and LiNi<sub>x</sub>Mn<sub>x</sub>Co<sub>1-2x</sub>O<sub>2</sub>. On the contrary, second type of cathode materials are the ones having relatively open structures such as manganese oxides, vanadium oxides and transition metal phosphates like olivine LiFePO<sub>4</sub>.

Three fundamental requirements for functional electrodes are indicated by Ying Wang and Guozhong Cao, as: (1) a high specific charge and charge density, that is, a high number of available charge carriers per mass and volume unit of the material; (2) a high cell voltage, resulting from a high (cathode) and low (anode) standard redox potential of the respective electrode redox reaction; and (3) a high reversibility

of electrochemical reactions at both cathodes and anodes to maintain the specific charge for hundreds of charge–discharge cycles [12]. Besides these, many other properties like safety, low cost, high electronic and ionic conductivity can be added to the requirements list. Even though the most important requirements have been determined for the electrode materials, a cathode material with the optimum properties has not been produced yet. For example, while current second type cathode materials have benefits like better safety and lower cost, they display lower energy densities than that of the first type cathode materials. Thus, either safety should be increased and cost should be decreased for the first type or energy density should be improved for the second type of cathode materials.

It is also known that properties such as capacity, cyclic stability, rate capability and energy density can be enhanced by decreasing particle size of the cathode materials due to the reduced charge transfer resistance, bigger surface area, freedom for volume change during charge-discharge cycles and short mass-charge diffusion distance [13, 14]. As a result, a second type of cathode material, nanosized lithium manganese silicate ( $\text{Li}_2\text{MnSiO}_4$ ) with carbon coating can be a good alternative for its benefits like theoretical ability of intercalation/extraction of two lithium ions per formula unit (which may provide higher energy densities from the formerly used second type of cathode materials), relatively lower cost, safety and less volume distortion while usage.



### 3 . PRINCIPLES OF CHARACTERIZATION METHODS

Main principles of the characterization methods used in this study are briefly explained under this paragraph.

#### 3.1 Thermogravimetric Analysis (TGA)

Working principle of thermogravimetric analysis (TGA) depends on mass change of the samples, related to the reactions with controlled environment conditions and heat, during the process. TGA devices are basically consisted of a furnace, a thermocouple and a balance (Figure 3.1.). Mass change can both be measured as a function of time and temperature. Main parameters of the TGA measurements can be indicated as heating rate, flow rate, crucible type and gas atmosphere (for e.g. nitrogen or air). Degradation of the samples can be observed as mass loss while mass increment usually points out a reaction of samples with the gas atmosphere [15].

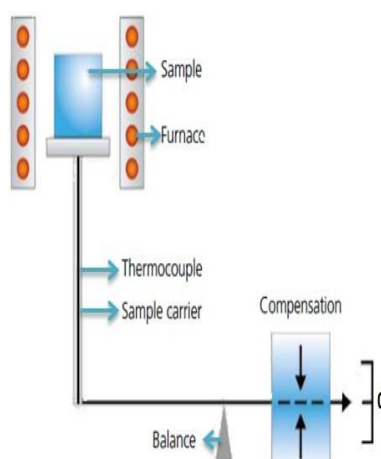


**Figure 3.1.** Diagram of TGA devices.

#### 3.2 X-ray Powder Diffraction (XRD)

Working principle of the X-ray diffraction measurements depends on the ability of crystals to reflect X-ray beams from their cleavage faces at certain angles of incidence (theta). This situation can be explained with the Bragg's Law (3.2); for

which  $\theta$  represents the reflection angle,  $d$  is the atomic layer distance in crystals,  $\lambda$  is the wavelength of incident X-ray beam and  $n$  is an integer.

$$n \lambda = 2d \sin \theta \quad (3.2)$$

XRD devices are basically consisted of a light source, aperture and detector slits, a monochromator, and a detector (Figure 3.2.). They can be used to examine any kind of crystal structure in all states of matter by using electron, proton, neutron or ion beams with a wavelength similar to the distance between molecular or atomic structures. Information about crystal structure of an unknown material, orientation of a single crystal or a grain and average spacing between layers or rows of atoms can be obtained from XRD measurements. Besides these shape, size and internal stress of a region can also be known from the XRD measurements for crystalline regions [16].

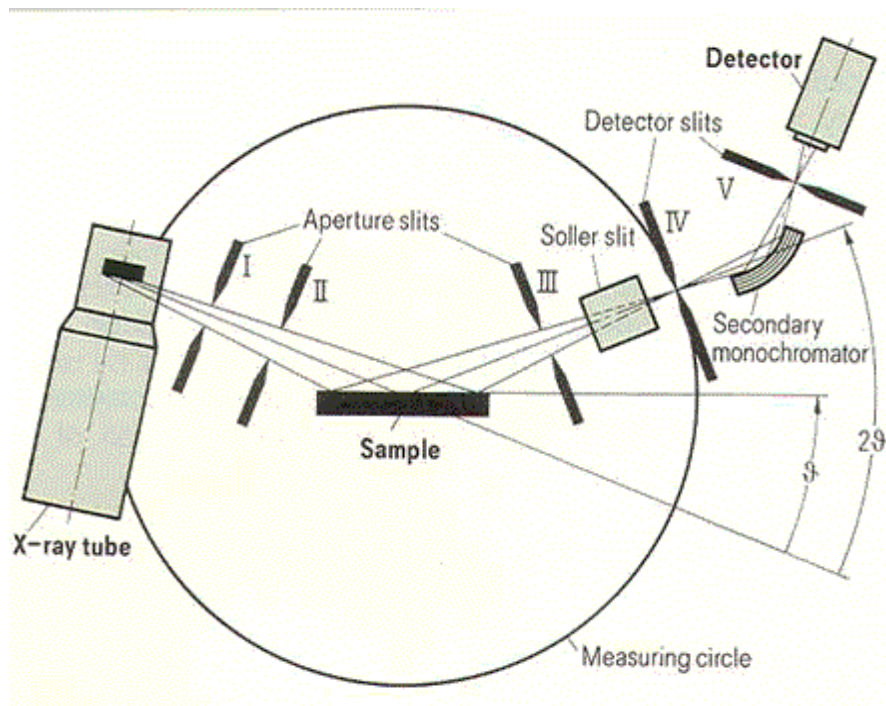


**Figure 3.2.** Diagram of XRD devices.

### 3.3 X-ray Photoelectron Spectroscopy (XPS)

X-ray photoelectron spectroscopy measurements depend on detection of the electrons ejected from a surface by the irradiation caused by monoenergetic soft x-rays. XPS devices are basically consisted of an X-ray source, an electron analyzer and a detector (Figure 3.3.).

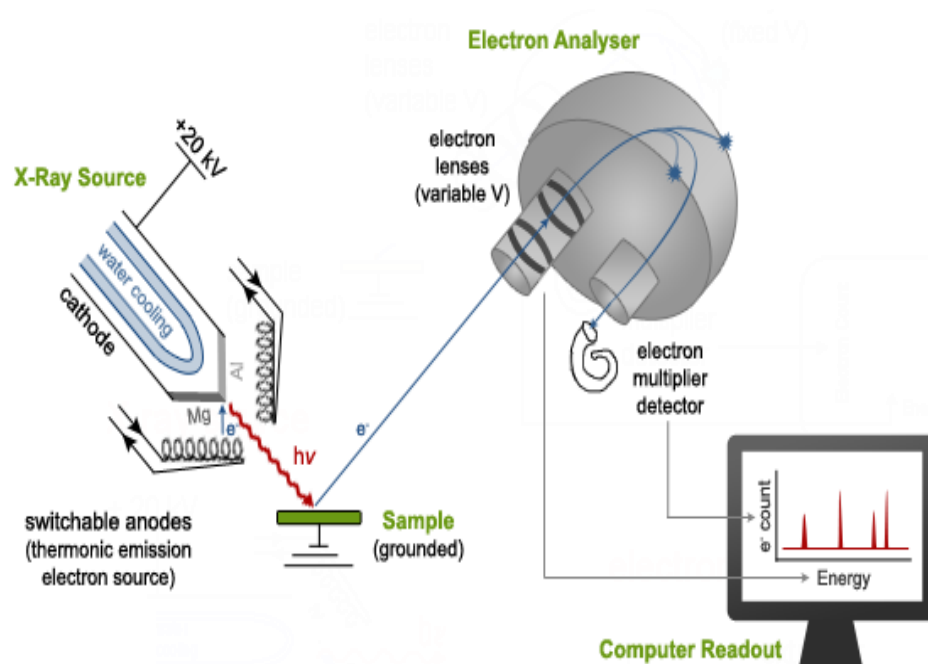


**Figure 3.3.** Diagram of an XPS system.

Measurements can be done for both conductive and insulating materials. Kinetic energies of the ejected photoelectrons can be used to identify the elements in the sample while photoelectron intensities can be used to determine the relative concentration of the elements. Furthermore; variation in the chemical shifts or binding energies of the photoelectron lines can be used to determine the chemical states and chemical state distribution of the samples [17, 18].

### 3.4 Conductivity Measurement

An alternating current (I) is applied to two active electrodes at an optimal frequency to measure the potential (V). Afterwards, conductance is measured by dividing I to measured V. And finally, cell constant is multiplied with the measured conductance in order to calculate the conductivity of the sample. In 4-probe cells an alternating current is applied to the outer rings (1 and 4) in order to provide a constant potential difference between the inner rings (2 and 3) (Figure 3.4.). Due to the negligible current of the voltage measurement, inner electrodes ( $R_2 = R_3 = 0$ ) are not polarized. Thus, the conductivity is directionally proportional to the applied current. Since the sample volume is certainly known for the measurements, 4-probe cells with an outer tube minimizes the beaker field effect [19].

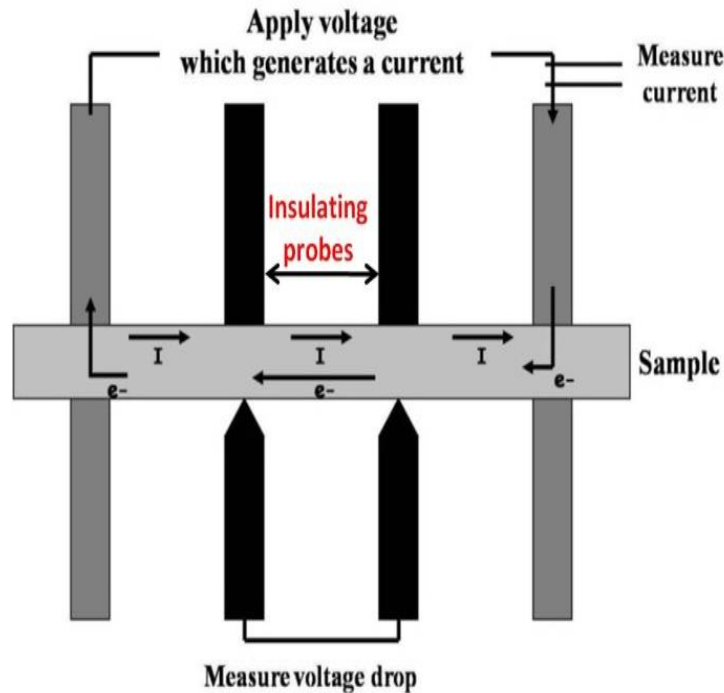


**Figure 3.4.** Diagram of a 4 point probe tester.

### 3.5 Differential Scanning Calorimetry (DSC)

Working principle of differential scanning calorimetry measurements depends on keeping the temperature rise/time constant for both sample vessel and the empty reference vessel in a certain temperature interval. Feedback control system, consisting of heaters and thermocouple controllers, is used to compare temperature of the reference vessel and arrange the heating rate of sample vessel according to the endothermic and exothermic reactions occurring in it (Figure 3.5.). When the sample gives an exothermic reaction, due to the extra heat occurring in the sample vessel, heating rate is decreased by the feedback control system and total temperature increase is kept similar with the temperature increase of the reference vessel during the reaction. Similarly when the sample gives an endothermic reaction, due to the extra consumption of heat in the sample vessel, heating rate is increased for the sample vessel and total temperature increase is kept similar with the temperature increase of reference vessel during the reaction. A graphic for heat output vs. achieved temperature is plotted for both heaters during the measurement in order to determine the state changes of the sample related to the temperature changes [15].

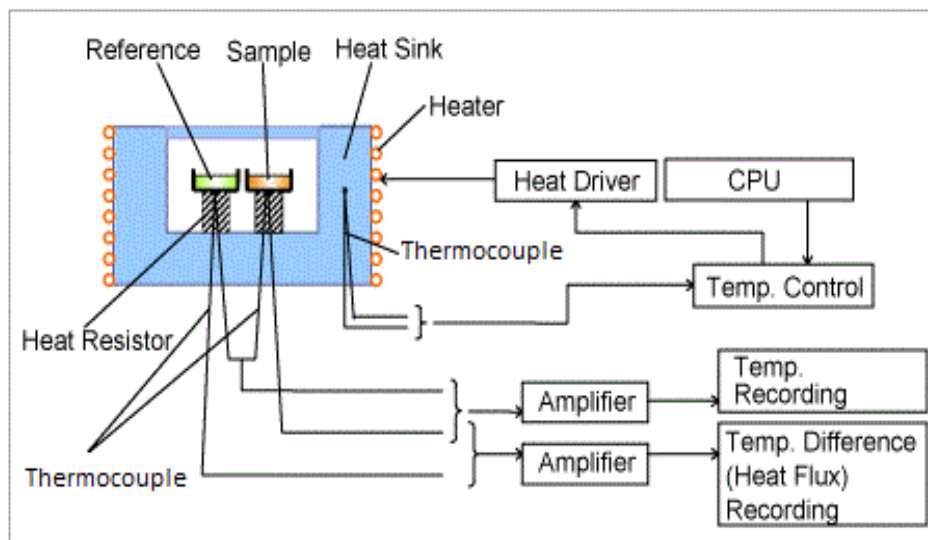


**Figure 3.5.** Diagram of a DSC device.



## **4 . EXPERIMENTAL PART**

### **4.1 Production of Pristine $\text{Li}_2\text{MnSiO}_4$ Powder**

#### **4.1.1 Preparation of the precursor**

Pechini type sol-gel synthesis was used for production of the  $\text{Li}_2\text{MnSiO}_4$ , using lithium acetate dehydrate (Aldrich), manganese acetate tetrahydrate (Aldrich), ethylene glycol (POCh), citric acid (POCh), ethanol (POCh) and tetraethoxysilane (TEOS, 98%, Aldrich) as starting reagents [7,8,9]. When the conditions indicated in the references are followed, it was possible to reach the proper stoichiometric composition with the help of chelating metal ions in the solution. Reactants were dissolved in gas reactor, in argon atmosphere and under a constant argon flow (flow rate: 5.7 l/h), with the molar ratio of 1:1:18:6:4:16 - Mn:Si:C<sub>2</sub>H<sub>6</sub>O<sub>2</sub>:C<sub>6</sub>H<sub>8</sub>O<sub>7</sub>:C<sub>2</sub>H<sub>5</sub>OH:H<sub>2</sub>O by using 20 wt.% excess amount of lithium acetate from stoichiometric amount, in order to produce a one-phase product. Fast and complete dissolution of metal acetates was accomplished by heating the solvent (water) up to 35 °C. Afterwards the obtained mixture was heated to 60 °C and polymerization of metal citrates was initiated with addition of a few drops of concentrated hydrochloric acid along with tetraethyl orthosilicate (TEOS) and ethylene glycol. After the reaction was conducted in a close reactor for 24 hours, obtained gel was first aged at 60 °C for 3 days in a closed reactor with argon atmosphere and then, in an air-drier at 60 °C for another 3 days.

#### **4.1.2. Calcination of the precursor gel**

After obtaining the precursor gel, it was placed on a gold crucible and calcined under argon atmosphere for 12 hours to thermally decompose the organic matrix. Argon flow was kept constant (flow rate: 30 ml/min.) throughout the calcination process and temperature was set to 800 °C (heating rate: 5°C/min.) which is high enough (<600 °C) to obtain the pure  $\text{Li}_2\text{MnSiO}_4$  phase (Pmn21), as indicated by Molenda et al [22].

### 4.1.3 Removal of the undesired carbon shell from the calcined sample

Purpose of the third step of pure  $\text{Li}_2\text{MnSiO}_4$  production is to remove the undesired carbon which remains around the  $\text{Li}_2\text{MnSiO}_4$  crystallites after the thermal decomposition of organic matrix [14, 21]. Sample is placed in a furnace on a gold crucible and kept at  $360^\circ\text{C}$  (heating rate:  $5^\circ\text{C}/\text{min.}$ ) for 6 hours under air atmosphere where air flow was kept constant (flow rate:  $150\text{ ml}/\text{min.}$ ) throughout the process (Figure 4.1.). It is known that the obtained sample has a partially oxidized layer around the crystallites because of the oxidation process of  $\text{Li}_2\text{MnSiO}_4$  [14].



**Figure 4.1.** Furnaces that are used for the  $\text{Li}_2\text{MnSiO}_4$  production.

### 4.1.4 Reduction

Last step of pure  $\text{Li}_2\text{MnSiO}_4$  production is the elimination of the oxidized layer around the crystallites (Figure 4.2.). For this purpose, sample was sealed in the middle of a quartz pipe by using quartz fibers, which was then placed into a furnace and kept at  $600^\circ\text{C}$  (heating rate:  $10^\circ\text{C}/\text{hour}$ ) for 1 hour under hydrogen and argon ( $\text{H}_2:\text{Ar} = 1:9$ , flow rate:  $50\text{ml}/\text{min.}$ ) atmosphere.

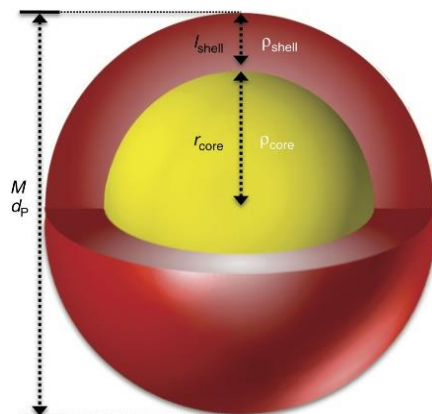


**Figure 4.2.** A core – shell figure where core represents the  $\text{Li}_2\text{MnSiO}_4$  crystallites and shell represents the oxidized layer.

## **4.2 Production of C/Li<sub>2</sub>MnSiO<sub>4</sub> Composites**

Preparation of the precursor, thermal decomposition/calcination of the precursor gel and removal of the undesired carbon from the calcined sample steps are done exactly the same as pristine Li<sub>2</sub>MnSiO<sub>4</sub> production.

### **4.2.1 Conductive carbon layer (CCL) coating**

Coating the electrode materials with conductive carbon layers by water impregnation process using hydrophilic polymers is a unique method, developed by J. Molenda and M. Molenda that aims to improve the cathode material properties and increase capacity of the batteries. Thus, water impregnation process is applied to the pristine cathode material according to this reference [13, 14]. Li<sub>2</sub>MnSiO<sub>4</sub> crystallites with partially oxidized shells, which were obtained after the third step, were coated with 10%, 15%, 20%, 25% and 30% of carbon where weight percentages are intentionally selected in order to determine the optimum carbon amount after comparison of the cell properties. Li<sub>2</sub>MnSiO<sub>4</sub> crystallites with partially oxidized shells were mixed and stirred in a plastic bowl with water solutions of pyromellitic acid (PMA) and Poly-N-vinylformamide (PNVF), until all of the water was evaporated and a mud-like mixture was obtained. Since only 20 wt.% of the carbon source (PNVF) can provide the coated carbon, 5 times the amount of Li<sub>2</sub>MnSiO<sub>4</sub> was added for PNVF and 5 wt.% of the total mass of PNVF was added for PMA. The process time had varied between 4 - 6 hours according to the amount of water and the carbon. Heating temperature was gradually increased while the process starting from 50 °C and kept below 100 °C to prevent the boiling. After enough water was evaporated to prevent sedimentation and grain agglomeration, obtained mud-like mixture is kept in a drying oven at 90 °C for 24 hours [14].

### **4.2.2 Pyrolysis**

After the drying process, polymer coated glassy sample was grinded. It is then placed into a furnace on a gold crucible and kept at 600°C (heating rate: 10°C/hour) for an hour under argon atmosphere. Argon flow was kept constant (flow rate: 30 ml/min.) throughout the pyrolysis process. Finally produced carbon coated C/Li<sub>2</sub>MnSiO<sub>4</sub> composites were grinded and cells are assembled by using the produced powders.

### 4.3 Characterization of the Cathode Materials

XRD patterns of both pristine, and C/Li<sub>2</sub>MnSiO<sub>4</sub> composite powders are examined using X-ray powder diffraction technique (XRD). Additionally, carbon coated samples are examined with thermogravimetric analysis (TGA) and electrical conductivity measurements (EC) are done for each of them. Furthermore, activation energies are calculated from the conductivity results.

Moreover, chemically delithiated pure Li<sub>2</sub>MnSiO<sub>4</sub> powders are examined by using X-ray photoelectron spectroscopy (XPS).

#### 4.3.1 Thermogravimetric analysis (TGA) and mass spectrometry (MS)

Thermogravimetric analyses (TGA) are applied to all carbon coated Li<sub>2</sub>MnSiO<sub>4</sub> powders, in order to determine the actual carbon in the composites and see if the actual carbon percentages are equal or similar to the theoretically calculated carbon amounts. Samples are placed in the thermoanalyzer (Thermostar GSD 300 T Balzers) in corundum crucibles (150 μl) in which they were heated up to 1000 °C (heating rate: 10°C/min.) under a constant air flow (flow rate: 80 ml/min). A quadrupole mass spectrometer (QMS), connected to the thermo-analyzer, is used to obtain information about evolved gases; on which mass lines were selected as 17 for OH, 18 for H<sub>2</sub>O and 44 for CO<sub>2</sub>.

Carbon and water percentages of the synthesized samples are determined from a graphic, plotted by using Origin Pro 9.1, where reference temperature (T<sub>r</sub>) was set as the X axis and weight percentage was set as the Y axis. Since water evaporation occurs before carbon starts burning, first slope can be attributed to the water evaporation and second slope can be attributed to the carbon oxidation.

#### 4.3.2 Preparation of the reference XRD patterns for Li<sub>2</sub>MnSiO<sub>4</sub>, LiMnSiO<sub>4</sub> and MnSiO<sub>4</sub>

First and foremost, most stable configurations of Li<sub>2</sub>MnSiO<sub>4</sub> are determined from the article of Dominko et al. as; Pmn2<sub>1</sub>, P2<sub>1</sub>/n and Pmnb structures [5]. Then, space groups for all three structures are determined from the “*Space Group Diagrams and Tables*” via the website of Birkbeck College, University of London. Finally, theoretical crystal morphologies and XRD patterns are obtained for Li<sub>2</sub>MnSiO<sub>4</sub>,

$\text{LiMnSiO}_4$  and  $\text{MnSiO}_4$  by using the proper space group information on *Mercury* program (Figure 4.3.) Reference XRD patterns are obtained for all three structures using two different methods (PBE-GGA and LSDA techniques) [24]. After the comparison of six reference  $\text{Li}_2\text{MnSiO}_4$  XRD patterns, it was clearly observed that  $\text{Pmn}2_1$  structure has the most similar XRD pattern to synthesized  $\text{Li}_2\text{MnSiO}_4$ , for both techniques (Figure 4.4.). Thus, it can be said that synthesized  $\text{Li}_2\text{MnSiO}_4$  has *orthorhombic  $\beta$* , structure.

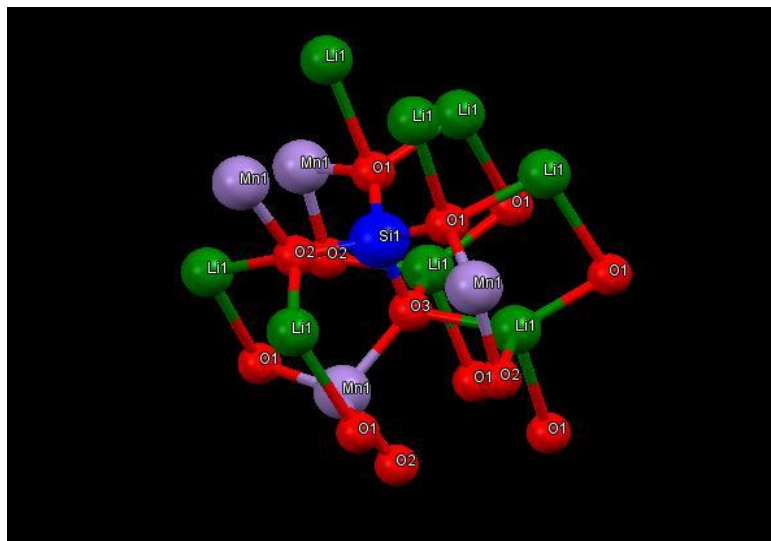


**Figure 4.3.** Theoretical  $\text{Li}_2\text{MnSiO}_4$  ( $\text{Pmn}2_1$ ) LSDA structure prepared by `Mercury` program.

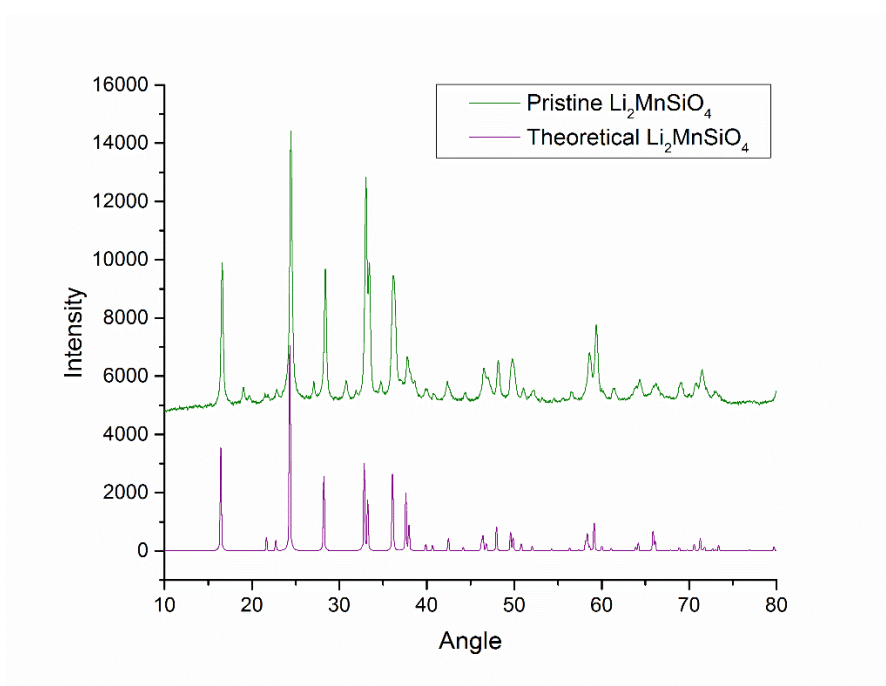


**Figure 4.4.** Comparison of the theoretical XRD patterns.

### 4.3.3 X-ray powder diffraction (XRD)

X-ray powder diffraction method is applied to obtain the XRD patterns of synthesized pure, and carbon coated  $\text{Li}_2\text{MnSiO}_4$  powders in order to prove that the syntheses occurred accurately. Besides this, samples after chemical delithiation processes are also examined by XRD method before the XPS analyses. A BRUKER D2 PHASER (using  $\text{Cu K}\alpha$  radiation =  $1.5418 \text{ \AA}$ ) device is used for the measurements with a scanning range of  $10\text{-}80^\circ$ .

Crystal structures and phases of the particles are determined from the comparison of XRD patterns of synthesized samples and theoretical XRD patterns of  $\text{Li}_2\text{MnSiO}_4$ .

Additionally, average crystallite sizes are calculated from the peaks with the highest intensities on XRD patterns. Widths of the peaks at their middle points are used in the Scherrer equation (4.1) in order to calculate the crystallite sizes.

$$d_{XRD} = \frac{K\lambda}{\beta \cos \theta} \quad (4.1)$$

On the Scherrer equation; 'd' represents the crystallite size where ,  $\lambda$  is the diffraction wavelength (in angstrom -  $\text{\AA}$ ),  $\beta$  is the calculated width at middle point of the peaks, K is the Scherrer constant value (related with the particle shape) and  $\theta$  is the diffraction angle of the peaks. Same four peaks, chosen from the reference XRD patterns, are used to calculate the crystallite sizes, and average crystallite sizes are shown in the table 5.1. along with the biggest and smallest grain sizes.

### 4.3.4 X-ray photoelectron spectroscopy (XPS)

X-ray Photoelectron Spectroscopy (XPS) method is applied to chemically oxidized samples, which had similar XRD patterns to  $\text{LiMnSiO}_4$  and  $\text{MnSiO}_4$ , in order to determine the delithiation level. Samples are placed in a high vacuum analytical chamber with the base pressure of  $5 \times 10^{-9}$  mbar and analyzed by using a Prevac photoelectron spectrometer with a hemispherical VG SCIENTA R3000 analyzer. XPS measurements were taken as read from the article of Molenda et al. [14], with a monochromatized aluminum source Al  $\text{K}\alpha$  ( $E = 1486.6 \text{ eV}$ ) and a low energy electron flood gun (FS40A-PS) to compensate charge on the surface during the measurements.

Peaks were recorded with a constant pass energy of 100 eV for the survey and high resolution spectra and binding energies were referenced on the Si 2p core level (102.0 eV). The composition and chemical surrounding of sample surface were investigated on the basis of the areas and binding energies of Si 2p, Mn 2p, C 1s, O 1s and Li 1s photoelectron peaks while fitting of the high resolution spectra was provided through the CasaXPS software.

#### 4.3.5 Conductivity and activation energy

Conductivities of the 10%, 15%, 20%, 25% and 30% carbon coated samples are measured by using the AC (33Hz) 4-probe technique (Sigma 1 in AC) within the temperature range of -20 °C and +40 °C, in order to determine the effect of carbon amount on conductivity of  $\text{Li}_2\text{MnSiO}_4$  samples. Considering elasticity of the materials related to carbon coatings, synthesized powders were pressed between two gold electrode discs ( $\varnothing=5$  mm) in a glass tube until they become pellet-like forms with approximately 1 mm thickness. Pressing level, which is important to obtain a stable resistivity, was determined according to the simultaneous resistance measurements.

For further comparison of carbon amounts, the Arrhenius Law (4.2) is used to calculate the activation energies ( $E_a$ ) by using the measured conductivities and results are shown in table 5.2.

$$\sigma = \sigma_0 \exp\left(-\frac{E_a}{K_B T}\right) \quad (4.2)$$

On Arrhenius equation  $E_a$  represents the activation energy where  $\sigma$  represents the measured conductivity of the materials,  $\sigma_0$  represents the pre-exponential factor, T represents the temperature and  $K_B$  represents the Boltzmann constant.

#### 4.3.6 Differential scanning calorimetry (DSC)

Differential scanning calorimetry (DSC) analyses were applied to the pure  $\text{Li}_2\text{MnSiO}_4$  sample, in order to determine chemical stability of the cathode material ( $\text{Li}_2\text{MnSiO}_4$ ) towards potential electrolyte solutions. Degradation of the electrolyte solutions under both air and argon atmospheres are also examined by DSC analyses. Since it is not desired for electrolyte solutions to react with cathode materials, most stable electrolytes are determined and used to prepare the coin cells.

A Mettler-Toledo 822° calorimeter with a cooling system (liquid nitrogen - LN<sub>2</sub>) is used for the experiments in which samples were placed in 40 µl aluminum crucibles. Argon flow was kept constant (80 ml/min) while temperature was increasing from 25 °C to 400 °C with a heating rate of 10 °C/min [14].

#### 4.4 Preparation of the Electrolyte Solutions

First and foremost, commonly used salts and solvents for lithium ion battery electrolyte solutions are determined with a literature research. Lithium hexafluorophosphate (LiPF<sub>6</sub>, Aldrich), lithium perchlorate (LiClO<sub>4</sub>, Aldrich), lithium bis(oxalato)borate (LiBOB, Aldrich) and lithium bis(trifluoromethanesulfonyl)imide (LiTFSI, Aldrich) were chosen as salts while; mixtures of ethylene carbonate (EC, Acros Organics), ethyl methyl carbonate (EMC, Aldrich), dimethyl carbonate (DMC, Sigma-Aldrich), diethyl carbonate (DEC, Acros Organics) and 1,1-dioxide tetramethylene sulfone (TMS, Aldrich) were chosen as the solvents. 1 M solutions of salts are prepared with each solvent mixture by having the same weight percentage for the solvents (Table 4.1.) [4, 25-31].

**Table 4.1.** Prepared Electrolyte Solutions.

	LiPF <sub>6</sub>	LiClO <sub>4</sub>	LiBOB	LiTFSI
EC:DEC	LiPF <sub>6</sub> w/ EC:DEC	LiClO <sub>4</sub> w/ EC:DEC	LiBOB w/ EC:DEC	LiTFSI w/ EC:DEC
EC:DMC	LiPF <sub>6</sub> w/ EC:DMC	LiClO <sub>4</sub> w/ DEC:DMC	LiBOB w/ EC:DEC	LiTFSI w/ EC:DEC
TMS:DEC	LiPF <sub>6</sub> w/ TMS:EMC	LiClO <sub>4</sub> w/ TMS:EMC	LiBOB w/ EC:EMC	LiTFSI w/ EC:EMC

In consideration of strong reaction of lithium compounds with air and moisture, all electrolyte solutions are prepared in a glove box under argon atmosphere.

#### 4.5 Chemical Delithiation

Reactions of pristine Li<sub>2</sub>MnSiO<sub>4</sub> nanoparticles with potential oxidizing agents are studied in order to prove the possibility of reversible exchange of up to two Li ions per formula unit while maintaining the crystallite structure. Hydrogen peroxide (Chempur), potassium persulfate (Sigma-Aldrich), sulfuric acid (Aldrich), and ammonia (Chempur) are chosen as the oxidizing agents after a literature research.

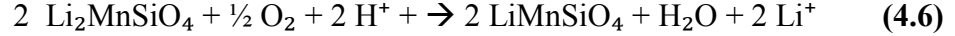
First oxidation reaction **(4.3)** was done using hydrogen peroxide (H<sub>2</sub>O<sub>2</sub>) as the oxidizing agent. Excess amount of H<sub>2</sub>O<sub>2</sub> (130 wt.%) is reacted with pristine Li<sub>2</sub>MnSiO<sub>4</sub> nanoparticles in acidic aqueous medium (CH<sub>3</sub>COOH + H<sub>2</sub>O) for 24 hours.



Second and third oxidation reactions were done using potassium persulfate (K<sub>2</sub>S<sub>2</sub>O<sub>8</sub>) as the oxidizing agent. For the second reaction **(4.4)**, excess amount of K<sub>2</sub>S<sub>2</sub>O<sub>8</sub> (130 wt.%) is reacted with pristine Li<sub>2</sub>MnSiO<sub>4</sub> nanoparticles in acidic aqueous medium (CH<sub>3</sub>COOH + H<sub>2</sub>O) for 24 hours. For the third oxidation reaction **(4.5)**, second reaction was repeated by using quintuple amount of K<sub>2</sub>S<sub>2</sub>O<sub>8</sub>.



Fourth and fifth oxidation reactions were done using sulfuric acid (H<sub>2</sub>SO<sub>4</sub>) as the oxidizing agent. For the fourth reaction **(4.6)**, excess amount of sulfuric acid H<sub>2</sub>SO<sub>4</sub> (130 wt.%) is reacted with pristine Li<sub>2</sub>MnSiO<sub>4</sub> nanoparticles in aqueous medium for 24 hours in order to remove one lithium ion from the structure.



For the fifth **(4.7)** oxidation reaction, fourth reaction was repeated by using double amount of H<sub>2</sub>SO<sub>4</sub> in order to remove both lithium ions from the structure.



Afterwards, pristine Li<sub>2</sub>MnSiO<sub>4</sub> nanoparticles were tried to be oxidized by heat treatment. Li<sub>2</sub>MnSiO<sub>4</sub> nanoparticles were gradually heated to 110°C and kept at 110°C in an oil bath for 24 hours in the designed experiment setup under constant oxygen flow **(4.8)** (Figure 4.5.).



Finally ammonia (NH<sub>3</sub>) was used as the oxidizing agent. pH of the aqueous medium was adjusted to 12 by adding enough NH<sub>3</sub>, and pristine Li<sub>2</sub>MnSiO<sub>4</sub> nanoparticles are kept in the alkaline medium for 24 and 72 hours **(4.9)**.



After the reactions, samples are centrifuged twice for 15 minutes, by using a Heraeus Megafube 40R type centrifuge produced by the Thermo SCIENTIFIC Company. Then, dried at 90°C for 24 hours in a Venticell type dryer produced by the BMT Company. Then, XRD measurements are done for dried samples and obtained patterns are compared with the theoretical XRD patterns of  $\text{Li}_2\text{MnSiO}_4$ ,  $\text{LiMnSiO}_4$  and  $\text{MnSiO}_4$ . Furthermore, XPS measurements are done for the samples that have matching XRD patterns with  $\text{LiMnSiO}_4$  and  $\text{MnSiO}_4$  in order to determine the accurate oxidation state of manganese (Mn).

#### 4.6 Electrochemical Oxidation/Delithiation

For the first set of experiments, 15% CCL  $\text{Li}_2\text{MnSiO}_4$  particles (coated on aluminum foils) were used as cathode material and 12 cells are assembled by using  $\text{LiPF}_6$  (EC:DEC),  $\text{LiPF}_6$  (EC:DMC),  $\text{LiPF}_6$  (TMS:EMC),  $\text{LiClO}_4$  (EC:DEC),  $\text{LiClO}_4$  (EC:DMC),  $\text{LiClO}_4$  (TMS:EMC), LiTFSI (EC:DEC), LiTFSI (EC:DMC), LiTFSI (TMS:EMC), LiBOB (EC:DEC), LiBOB(EC:DMC) and finally LiBOB(TMS:EMC) as the electrolyte solutions. The galvanostatic charge-discharge cycling studies were conducted in two electrode configuration using RC 2032 coin cell  $\text{Li/Li}^+(\text{C/Li}_2\text{MnSiO}_4)$  between 1.8 and 4.5 V at C/20 rate at room temperature conditions.

In the second set of experiments, electrolyte solutions which provided higher capacities for the previous batteries ( $\text{LiPF}_6$  w/EC:DMC and  $\text{LiPF}_6$  w/EC:DEC) are used to assemble batteries for cathode materials with carbon loadings of 10 wt.%, 15 wt.%, 20 wt.%, 25 wt.% and 30 wt.%. The galvanostatic charge-discharge cycling studies were conducted in two electrode configuration using RC 2032 coin cell type batteries  $\text{Li/Li}^+(\text{CCL/Li}_2\text{MnSiO}_4)$  between 1.8 and 4.5 V at C/50 at room temperature.

In the third set of experiments, optimum carbon loading amount (30%) to obtain the highest capacities is determined and twelve batteries are assembled with each electrolyte solution by using 30% C/ $\text{Li}_2\text{MnSiO}_4$  nanoparticles as the cathode material. The galvanostatic charge-discharge cycling studies were conducted in two electrode configuration using RC 2032 coin cell type batteries  $\text{Li/Li}^+(\text{C/Li}_2\text{MnSiO}_4)$  between 1.8 and 4.5 V at C/50 rate at room temperature conditions.

#### 4.6.1 Assembling of coin cell type batteries

A coin cell type battery is mainly consisted of a positive case, cathode and anode materials, a separator and a negative case (Figure 4.7.) First step of cell assembling is to place a seal on the positive case. Secondly, if the cathode material is a powder, an aluminum crucible should be placed in the middle of the positive case and 10-20 mg of powder should be placed in the aluminum crucible. On the other hand, powder cathode material can be coated on an aluminum foil and directly placed in the middle of the positive case without using an aluminum crucible. Afterwards, first a celgard then a watmann should be placed on the cathode material as separators, and both should be wetted with the electrolyte solution (6 or 7 drops). Next, anode material, which is placed on the metal spacer, should be put on the wet watmann separator. Finally a spring should be added and cell should be closed by using a negative case. Cells should be pressed in order to prevent any air leakage and provide maximum contact between the cell components.

As previously mentioned,  $\text{Li}_2\text{MnSiO}_4$  is used as the cathode material in this study and lithium metal is used as the anode material with various electrolyte solutions. In consideration of strong reaction of lithium compounds with air and moisture, all batteries are assembled in a glove box, under argon atmosphere.



**Figure 4.5.** Components of a coin cell.

#### **4.6.2 Disassembling of coin cell type batteries**

After the second set of electrochemical delithiation experiments, battery with the highest observed capacity (cell prepared from C/Li<sub>2</sub>MnSiO<sub>4</sub> nanocomposite containing 30 wt.% of carbon and 1M LiPF<sub>6</sub> in EC:DMC electrolyte solution) is assembled again and after the first charging step, put back into the glove box. Totally charged/delithated cathode material (Li<sub>2</sub>MnSiO<sub>4</sub>) is taken out of the coin cell by using a nipper tool. Afterwards cathode material is dried under vacuum and XPS measurement is done to determine the actual oxidation state of the Mn in the sample.

## 5. RESULTS AND DISCUSSIONS

### 5.1 Comparison of the XRD Patterns of Synthesized Cathode Materials

It is proved from the XRD pattern comparison that,  $\text{Li}_2\text{MnSiO}_4$  nanoparticles could be properly synthesized by using Pechini type sol-gel synthesis. Furthermore it is proved that, carbon coating by water impregnation process do not change the crystal structure of the synthesized nanocomposite cathode materials (Figure 5.1).

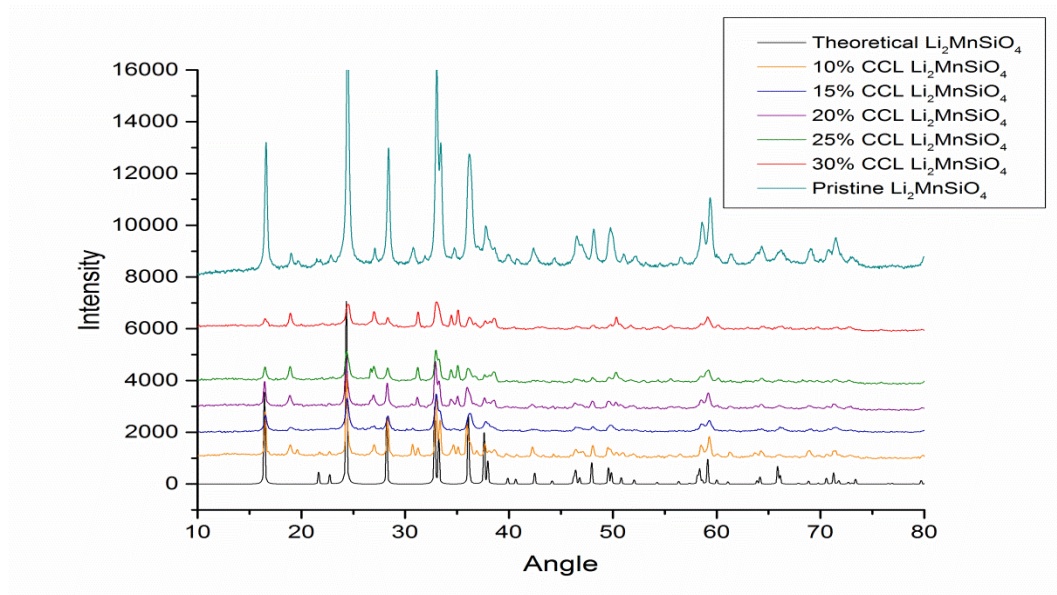


**Figure 5.1.** XRD patterns of theoretical and synthesized  $\text{Li}_2\text{MnSiO}_4$  and  $\text{C}/\text{Li}_2\text{MnSiO}_4$  samples.

Crystallite sizes are also calculated from the XRD patterns for each sample and shown on the table given below (Table 5.1.). Despite of the slight agglomeration of 10%  $\text{C}/\text{Li}_2\text{MnSiO}_4$ , it is possible to say that there is no crystallite growth during carbon coating process.

**Table 5.1.** Crystallite sizes of the synthesized cathode materials.

Carbon Percentage	0%	10%	15%	20%	25%	30%
Average size (nm)	45	61	42	46	36	39

## 5.2 Conductivity and Activation Energy Results

Measured conductivities of the synthesized and carbon coated cathode materials are compared for 10%, 15%, 20%, 25% and 30% C/Li<sub>2</sub>MnSiO<sub>4</sub>. Afterwards, activation energies are calculated for each sample by using measured conductivities and Arrhenius Law (4.2). Conductivity of the 10% C/Li<sub>2</sub>MnSiO<sub>4</sub> composite was measured as  $2.21 \times 10^{-3}$  S/cm and activation energy of the sample is calculated as 0.041 eV (Figure 5.2.).

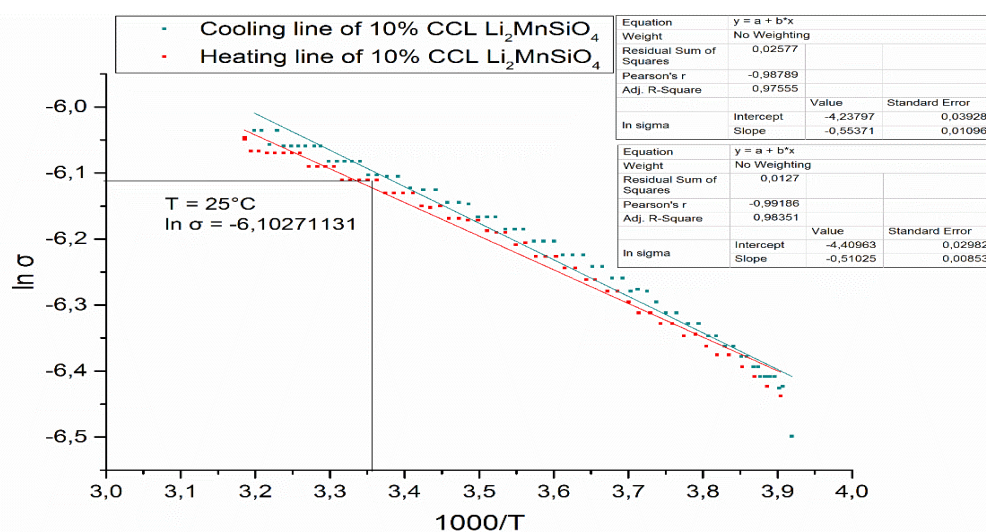


**Figure 5.2.** Conductivity graphic of 10% C/Li<sub>2</sub>MnSiO<sub>4</sub>.

Conductivity of the 15% C/Li<sub>2</sub>MnSiO<sub>4</sub> nanocomposite was measured as  $0.75 \times 10^{-5}$  S/cm and activation energy of the sample is calculated as 0.074 eV (Figure 5.3.).

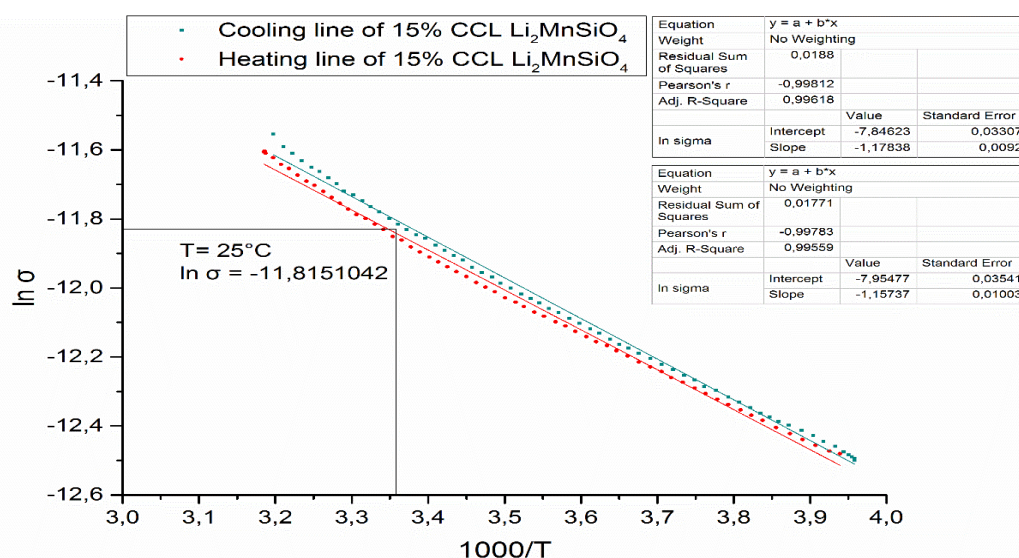


**Figure 5.3.** Conductivity graphic of 15% C/Li<sub>2</sub>MnSiO<sub>4</sub>.

Conductivity of the 20% C/Li<sub>2</sub>MnSiO<sub>4</sub> nanocomposite was measured as  $1.32 \times 10^{-5}$  S/cm and activation energy of the sample is calculated as 0.089 eV (Figure 5.4).

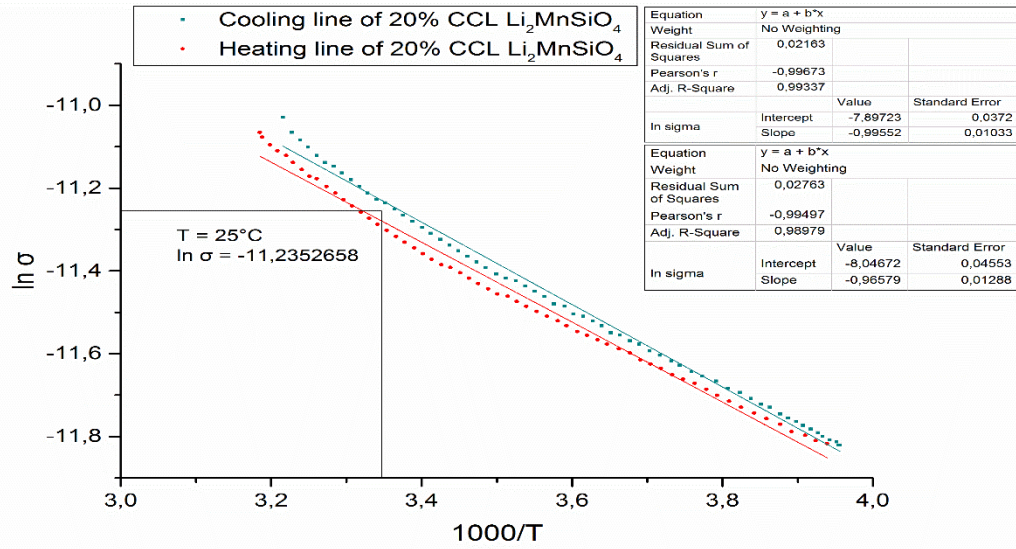


**Figure 5.4.** Conductivity graphic of 20% C/Li<sub>2</sub>MnSiO<sub>4</sub>.

Conductivity of the 25% C/Li<sub>2</sub>MnSiO<sub>4</sub> nanocomposite was measured as  $2.38 \times 10^{-5}$  S/cm and activation energy of the sample is calculated as 0.077 eV (Figure 5.5.).

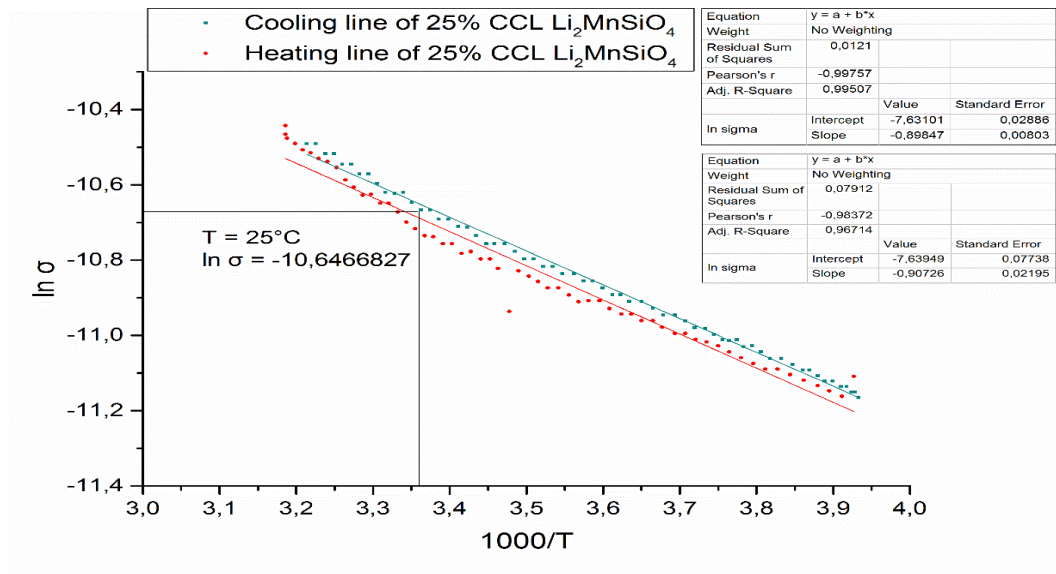


**Figure 5.5.** Conductivity graphic of 25% C/Li<sub>2</sub>MnSiO<sub>4</sub>.

And finally, conductivity of the 30% C/Li<sub>2</sub>MnSiO<sub>4</sub> nanocomposite was measured as  $2.81 \times 10^{-5}$  S/cm and activation energy of the sample is calculated as 0.098 eV (Figure 5.6.).

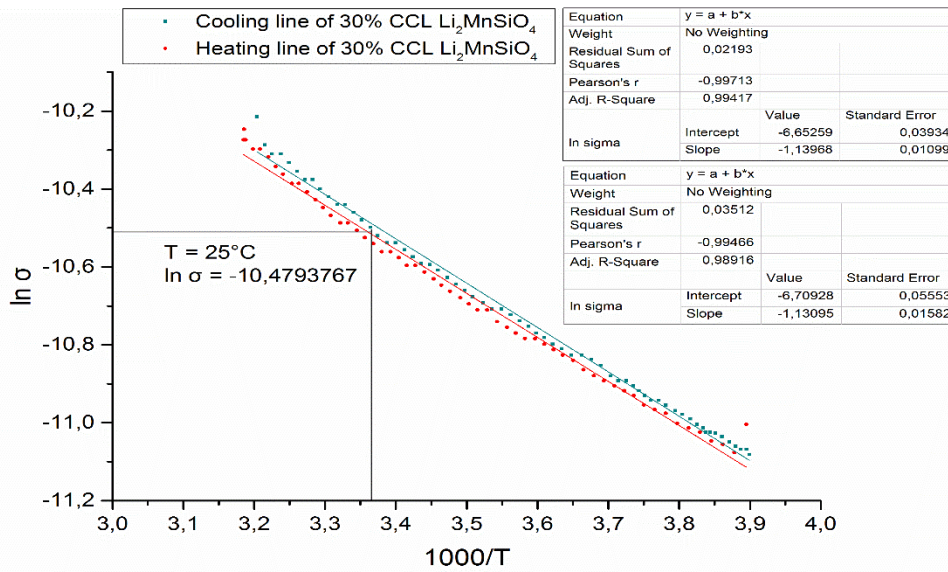


**Figure 5.6.** Conductivity graphic of 30% C/Li<sub>2</sub>MnSiO<sub>4</sub>.

Except for the 10% C/Li<sub>2</sub>MnSiO<sub>4</sub>, conductivity results showed that conductivity is increased with the increase in the carbon amount in the composites (Table 5.2.).

**Table 5.2.** Conductivity and activation energy values vs. carbon content.

Carbon Percentage (%)	10	15	20	25	30
Conductivity (S/cm)	2.21x10 <sup>-3</sup>	0.75x10 <sup>-5</sup>	1.32 x10 <sup>-5</sup>	2.38x10 <sup>-5</sup>	2.81x10 <sup>-5</sup>
Activation Energy (eV) [cooling]	0.048	0.102	0.086	0.075	0.098
Activation Energy (eV) [heating]	0.044	0.100	0.082	0.078	0.098

### 5.3 TGA Results

Actual carbon amounts in the composite cathode materials (C/Li<sub>2</sub>MnSiO<sub>4</sub>) are determined for theoretically 10%, 15%, 20%, 25% and 30% C/Li<sub>2</sub>MnSiO<sub>4</sub> samples. A very slight percentage difference, compared to the theoretical carbon content, is observed for each sample due to the inhomogeneous mixing of Poly-N-vinylformamide (PNVF) and pyromellitic acid (PMA) while the water impregnation processes. Water amount adsorbed on the synthesized cathode materials are determined from the first, relatively slight mass changes while carbon amounts are determined from the second temperature range that show rapid mass decrements.

Actual carbon amount is calculated as 11.1% for the theoretically 10% C/Li<sub>2</sub>MnSiO<sub>4</sub> while the calculated water amount is 2.4% and active material amount is 86.5% for it (Figure 5.7.).

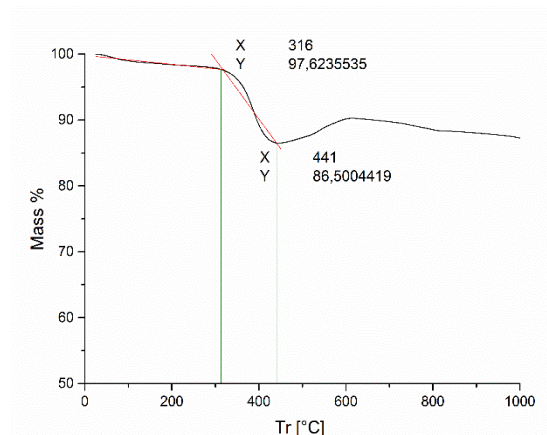


**Figure 5.7.** TGA graphic of theoretically 10% C/Li<sub>2</sub>MnSiO<sub>4</sub>.

Similarly, actual carbon amount is calculated as 15.2% for the theoretically 15% C/Li<sub>2</sub>MnSiO<sub>4</sub> while the calculated water amount is 5.6% and active material amount is 79.1% for it. Afterwards, actual carbon amount is calculated as 21.5% for the theoretically 20% C/Li<sub>2</sub>MnSiO<sub>4</sub> while the calculated water amount is 2.4% and active material amount is 74.6% for it (Figure 5.8.). Furthermore, actual carbon amount is calculated as 22.5% for the theoretically 25% C/Li<sub>2</sub>MnSiO<sub>4</sub> while the calculated water amount is 7.5% and active material amount is 70.1% for it. And finally, actual carbon amount is calculated as 29.9% for the theoretically 30% C/Li<sub>2</sub>MnSiO<sub>4</sub> while the calculated water amount is 8.3% and active material amount is 61.7% for it (Figure 5.9.).

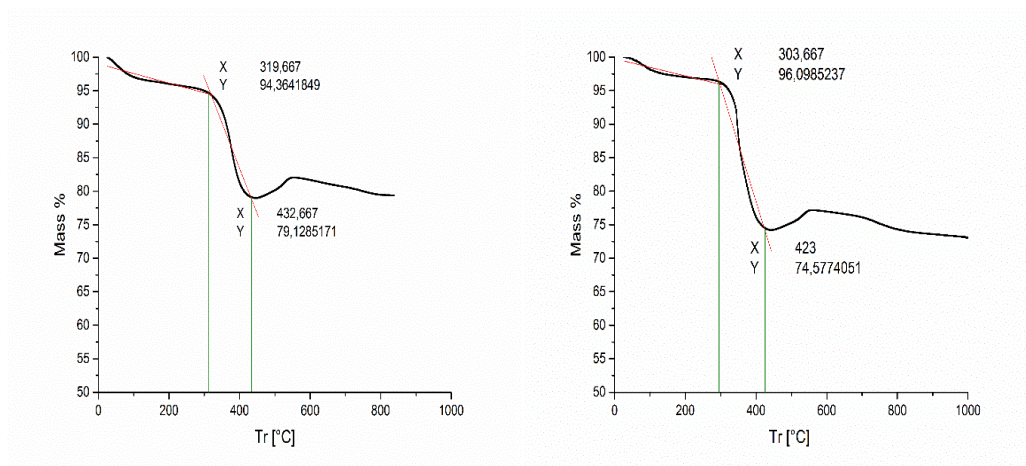


**Figure 5.8.** TGA graphics of theoretically 15% (left) and 20% (right) C/Li<sub>2</sub>MnSiO<sub>4</sub>.

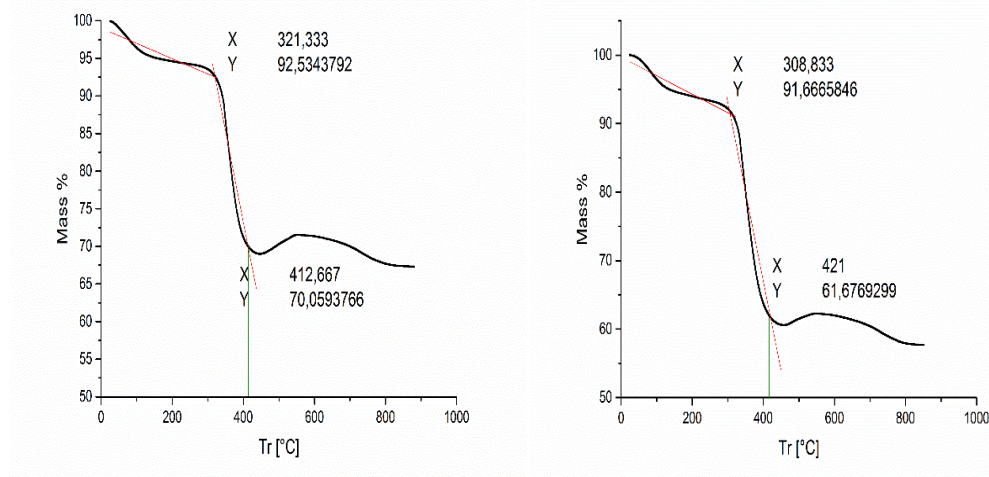


**Figure 5.9.** TGA graphics of theoretically 25% (left) and 30% (right) C/Li<sub>2</sub>MnSiO<sub>4</sub>.

Even though carbon content in the composite cathode materials are not exactly the same with the theoretical amounts, they were very close to the expected amounts. Thus it is possible to say from the TGA results that, water impregnation process is a precise method to coat the Li<sub>2</sub>MnSiO<sub>4</sub> nanoparticles with desired amount of carbon (Table 5.3.).

**Table 5.3.** Theoretical and actual carbon contents

Theoretical Carbon Content (%)	10	15	20	25	30
Actual Carbon Content (%)	11.1	15.2	21.5	22.5	29.9

#### 5.4 Chemical Oxidation/Delithiation Results

First of all; theoretical XRD patterns of LiMnSiO<sub>4</sub> and MnSiO<sub>4</sub> are compared with the XRD patterns obtained from materials after the reactions of cathode material (Li<sub>2</sub>MnSiO<sub>4</sub>) with hydrogen peroxide (H<sub>2</sub>O<sub>2</sub>), potassium persulfate (K<sub>2</sub>S<sub>2</sub>O<sub>8</sub>), sulfuric acid (H<sub>2</sub>SO<sub>4</sub>) and ammonia (NH<sub>3</sub>). Same comparison is also done for the heat treated cathode material. Afterwards, XPS analysis are done for the samples that show similar XRD patterns to LiMnSiO<sub>4</sub> and MnSiO<sub>4</sub>, in order to determine the actual oxidation level of manganese in the cathode materials.

### 5.4.1 XRD results

It is observed from the XRD pattern comparison that, cathode material was decomposed because of the reaction with hydrogen peroxide ( $\text{H}_2\text{O}_2$ ) for 24 hours in acidic medium. The crystalline structures that occurred after decomposition could not be determined from the database ICDD-PDF4+ (Figure 5.10.). Thus it can be said that, reacting with  $\text{H}_2\text{O}_2$  is not appropriate to perform the chemical delithiation of the cathode material ( $\text{Li}_2\text{MnSiO}_4$ ) under these circumstances.

It is observed from the XRD pattern comparison that, cathode material was partially oxidized along with partial decomposition of the crystalline structure because of the reaction with 1M potassium persulfate ( $\text{K}_2\text{S}_2\text{O}_8$ ) for 24 hours in acidic medium (Figure 5.11.). XPS measurement is done for the further investigation.

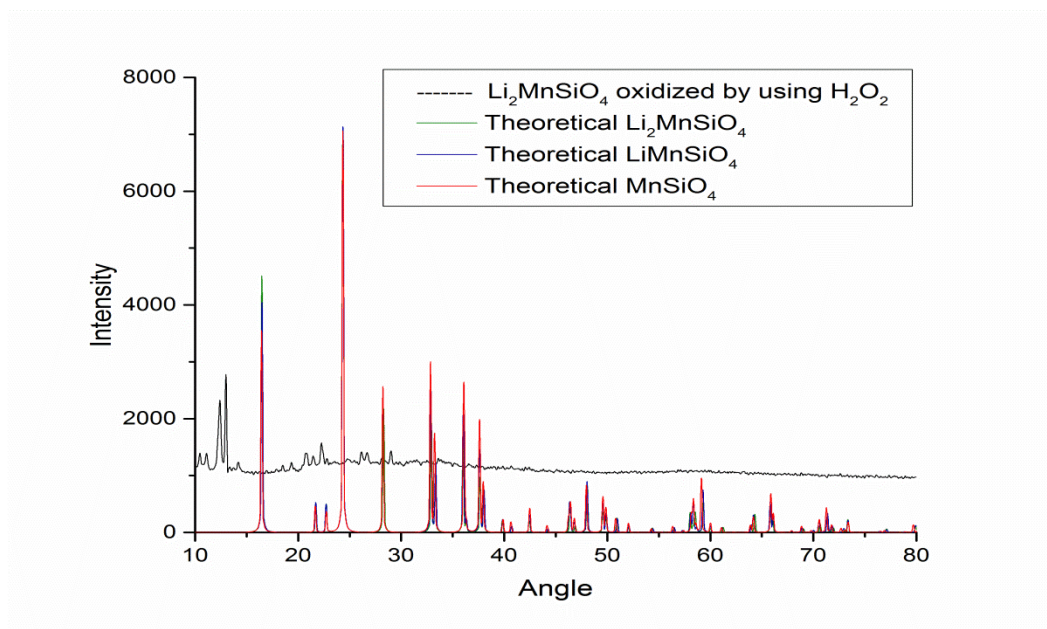


**Figure 5.10.** XRD comparison graphic for the sample oxidized using  $\text{H}_2\text{O}_2$ .

It is observed from the XRD pattern comparison that, cathode material was decomposed into potassium lithium sulfate ( $\text{KLi}(\text{SO}_4)$ ) and an amorphous phase containing Mn and Si because of the reaction with 5M potassium persulfate ( $\text{K}_2\text{S}_2\text{O}_8$ ) for 24 hours in acidic medium (Figure 5.12.). Thus it can be said that it is not possible to chemically delithiate the cathode material ( $\text{Li}_2\text{MnSiO}_4$ ) under these circumstances.

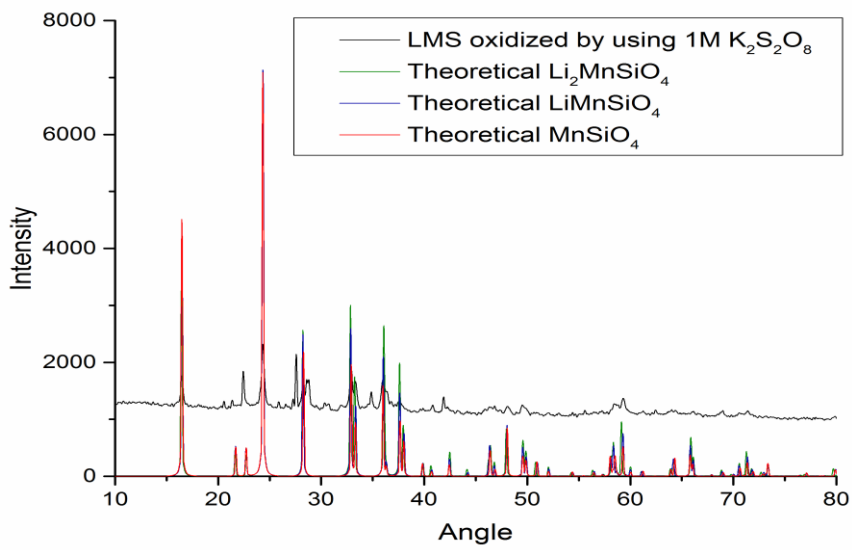


**Figure 5.11.** XRD comparison graphic for the sample oxidized using 1M  $K_2S_2O_8$ .

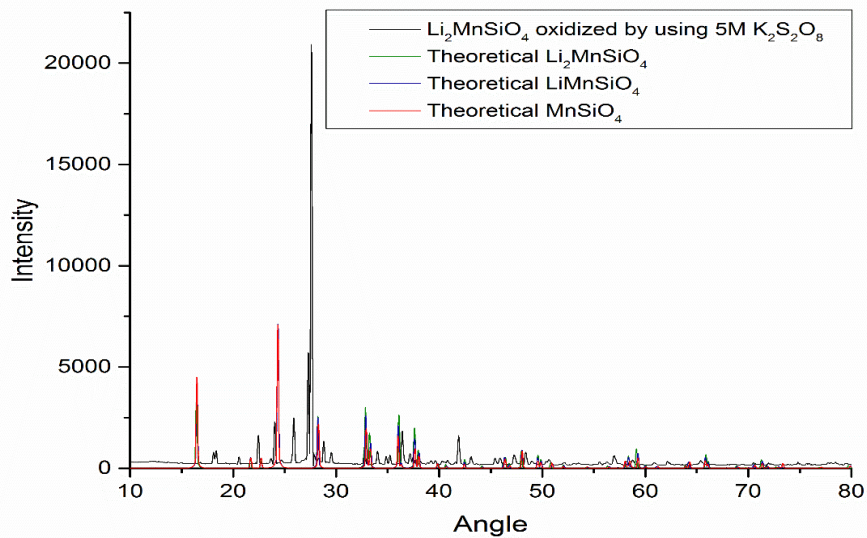


**Figure 5.12.** XRD comparison graphic for the sample delithiated using 5M  $K_2S_2O_8$ .

It is observed from the XRD pattern comparison that, cathode material was decomposed into an amorphous material because of the reaction with 1M sulfuric acid ( $H_2SO_4$ ) for 24 hours under oxygen flow (Figure 5.13). Thus it can be said that it is not possible to chemically delithiate the cathode material ( $Li_2MnSiO_4$ ) under these circumstances.

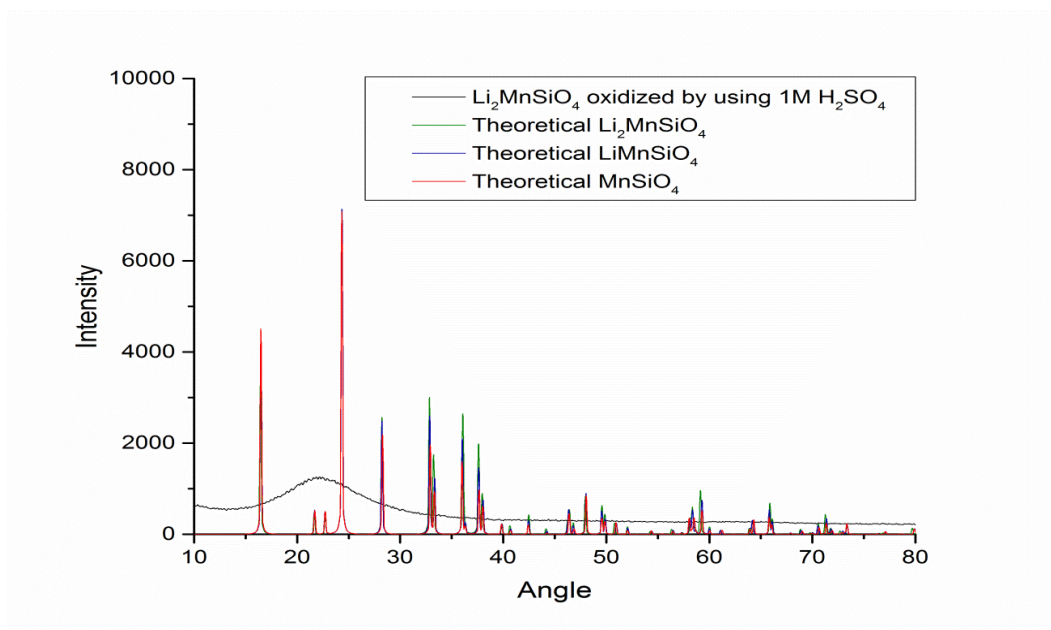


**Figure 5.13.** XRD comparison graphic for the sample oxidized using 1M H<sub>2</sub>SO<sub>4</sub>.

It is observed from the XRD pattern comparison that, cathode material was decomposed into manganese silicate (MnSiO<sub>4</sub>) and an amorphous phase of Mn because of the reaction with 2M sulfuric acid (H<sub>2</sub>SO<sub>4</sub>) for 24 hours under oxygen flow (Figure 5.14.). Thus it can be said that it might be possible to chemically delithiate some of the cathode material (Li<sub>2</sub>MnSiO<sub>4</sub>) under these circumstances.

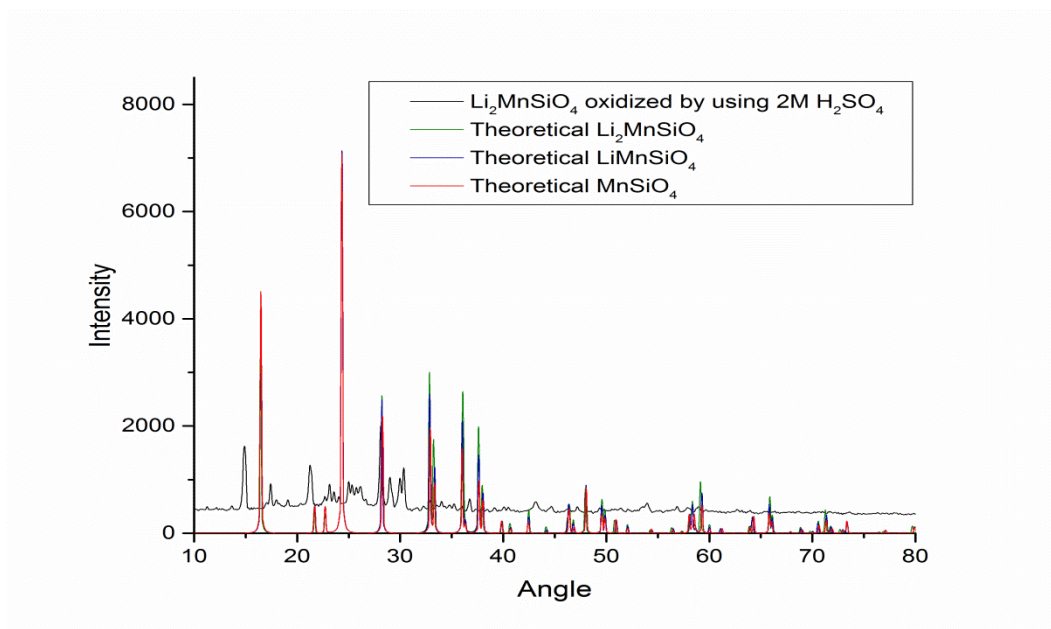


**Figure 5.14.** XRD comparison graphic for the sample oxidized using 2M H<sub>2</sub>SO<sub>4</sub>.

A similar XRD pattern to LiMnSiO<sub>4</sub> and MnSiO<sub>4</sub> is obtained for the sample after heat treatment for 30 minutes (Figure 5.15.). Thus, a further XPS measurement is

done for this cathode material in order to determine the oxidation level of manganese. On the contrary, sample which was obtained after heat treatment for 24 hours was decomposed into another material (Figure 5.16.). Thus it is possible to say that, 24 hours is too long to delithiate  $\text{Li}_2\text{MnSiO}_4$  by heat treatment.

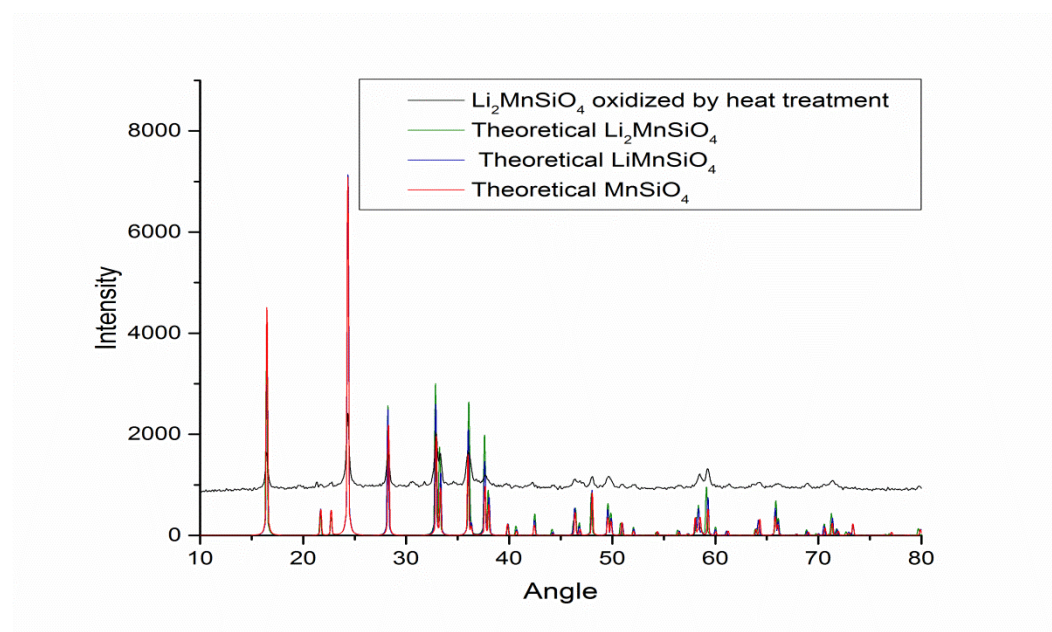


**Figure 5.15.** XRD comparison graphic for the sample oxidized by heat treatment for 30 minutes.

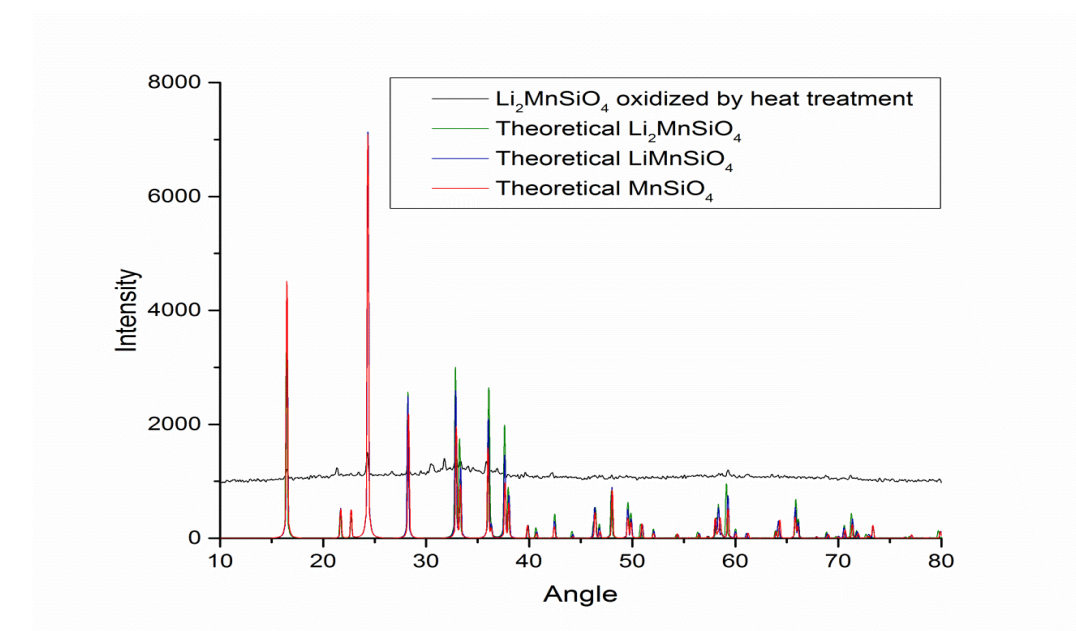


**Figure 5.16.** XRD comparison graphic for the sample oxidized by heat treatment for 24 hours.

XRD pattern of the sample which is delithiated using ammonia ( $\text{NH}_3$ ) for 24 hours was similar to the XRD patterns of  $\text{LiMnSiO}_4$  and  $\text{MnSiO}_4$  (Figure 5.17.). Thus,

XPS measurements are done in order to determine the oxidation level of manganese in the cathode materials reacted with  $\text{NH}_3$ .

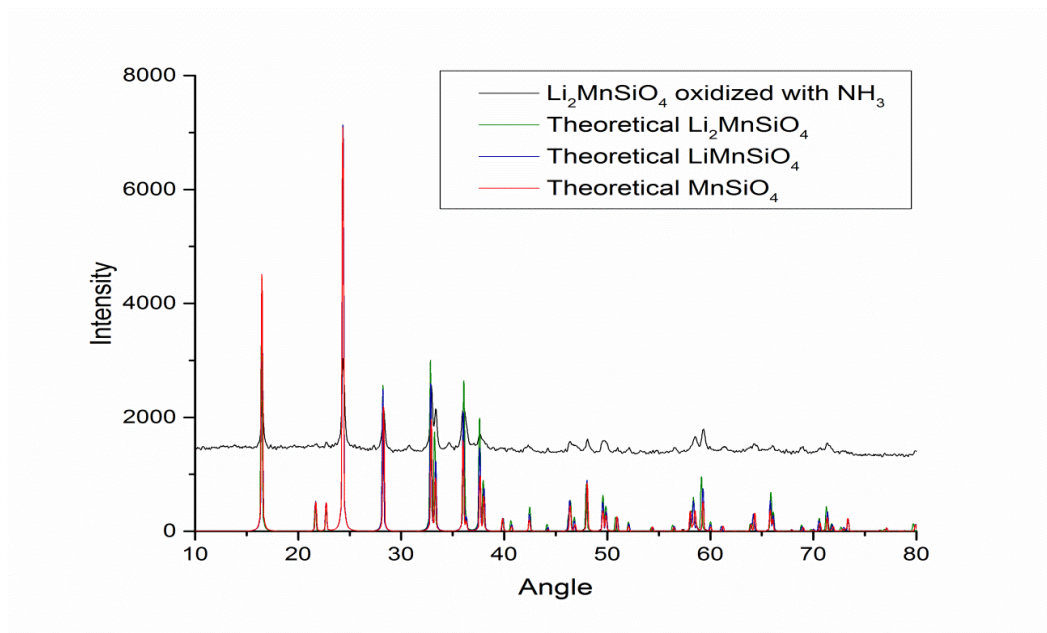


**Figure 5.17.** XRD comparison graphic for the sample oxidized using  $\text{NH}_3$  for 24 hours.

It is observed from the XRD pattern comparison that, cathode material was completely decomposed into an amorphous material because of the reaction with  $\text{NH}_3$  for 72 hours (Figure 5.18.). Thus even it is possible to chemically delithiate the

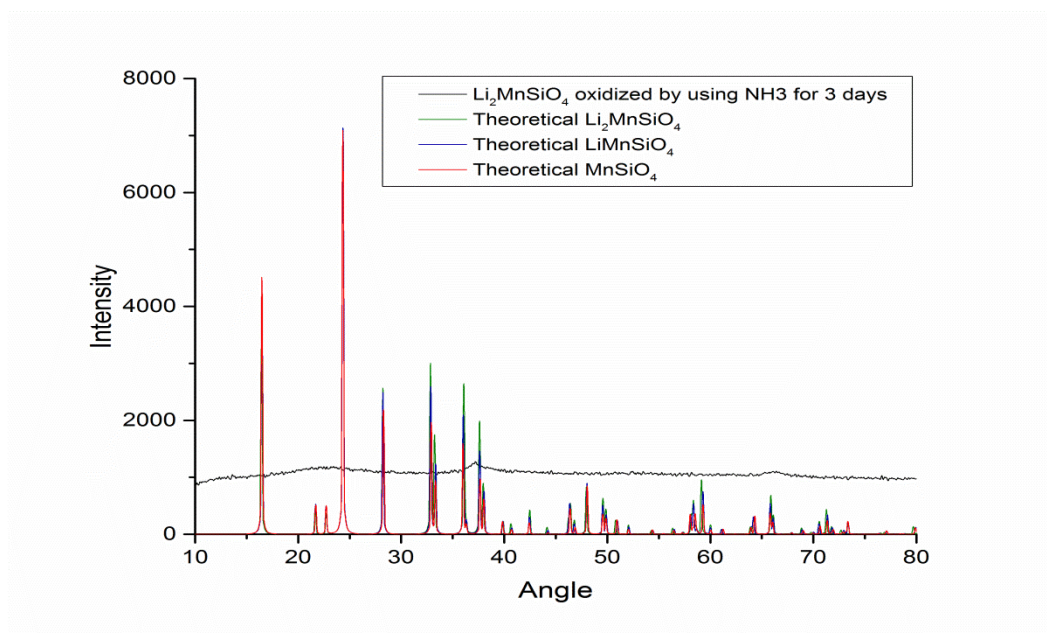


**Figure 5.18.** XRD comparison graphic for the sample oxidized using  $\text{NH}_3$  for 72 hours.

cathode material ( $\text{Li}_2\text{MnSiO}_4$ ) under these circumstances, this irreversible method is not appropriate to prove the chemical oxidation of  $\text{Li}_2\text{MnSiO}_4$  particles.

#### 5.4.2 XPS results

Average oxidation state of manganese (Mn) is calculated for the chemically delithiated cathode materials ( $\text{Li}_2\text{MnSiO}_4$ ) by using the binding energy data obtained from the XPS measurements.

Average oxidation state of manganese (Mn) is calculated as 2.10 from XPS analysis for the  $\text{Li}_2\text{MnSiO}_4$  particles after heat treatment for 30 minutes. According to this result, most of the Mn exist on the second oxidation state while a very few amount of the Mn exist on the fourth oxidation state after the reaction. A possible reason for this situation is the Jahn-Teller distortions that occur during the lithiation/delithiation process to arrange the symmetry and energy of the tetrahedral structure [39]. This result also shows that the  $\text{LiMnSiO}_4$  structure is not stable thus the cathode material should be improved to preserve the structure during transitions while charging and discharging processes in order to obtain better performances for the batteries. Furthermore it should be indicated that, delithiation percentage is very low after heat treatment for 30 minutes. Thus, the method is not convenient.

Average oxidation state of manganese (Mn) is calculated as 2.28 from XPS analysis for the  $\text{Li}_2\text{MnSiO}_4$  particles after reacting with ammonia ( $\text{NH}_3$ ) for 24 hours. According to this result both of the lithium ions might be removed from the cathode material under these circumstances. But it is not possible to be certain about this information due to the partial decomposition of the sample since the products, which occurred after decomposition, might contain oxidized Mn that contribute to the average oxidation state of Mn measured by using XPS.

In conclusion it can be said that the pristine  $\text{Li}_2\text{MnSiO}_4$  samples could be partially delithiated by using potassium persulfate, ammonia and slightly via heat treatment for 30 minutes. Among the previously mentioned reactions, reacting with  $\text{K}_2\text{S}_2\text{O}_8$  shows a better performance as the oxidizing process.

Average oxidation state of manganese (Mn) is calculated as 2.52 from XPS analysis for the  $\text{Li}_2\text{MnSiO}_4$  particles after reacting with potassium persulfate ( $\text{K}_2\text{S}_2\text{O}_8$ ) for 24 hours (Figure 5.19.).

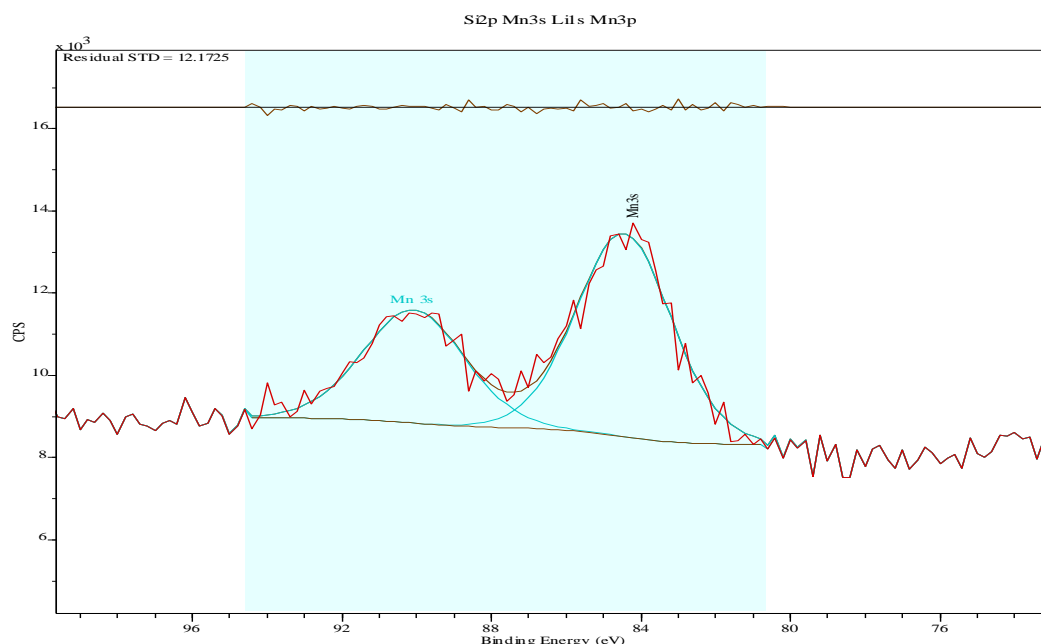


**Figure 5.19.** An example for the XPS graphics of oxidized  $\text{Li}_2\text{MnSiO}_4$  samples.

Similar to the oxidation with ammonium, most of the Mn species are on the second oxidation state while some Mn species also exist on the fourth oxidation state after the reaction. Even though the same Jahn-Teller distortions are observed during the lithiation/delithiation processes, it is possible to say that  $\text{K}_2\text{S}_2\text{O}_8$  showed a better performance, as an oxidizing agent, than the  $\text{NH}_3$  due to the occurrence of higher amount of Mn species on the fourth state of oxidation (Table 5.4.).

**Table 5.4.** XPS information of chemically oxidized  $\text{Li}_2\text{MnSiO}_4$

Sample	Mn 3s			Oxidation State
	BE (1)	BE (2)	$\Delta E$	
$\text{Li}_2\text{MnSiO}_4$ oxidized by $\text{NH}_3$	804.10	89.92	5.8	2.28
$\text{Li}_2\text{MnSiO}_4$ oxidized by 1M $\text{K}_2\text{S}_2\text{O}_8$	88.44	90.07	5.6	2.52

## 5.5 Electrochemical Oxidation/Delithiation Results

Data obtained from the galvanostatic charge-discharge tests are used to calculate the practical capacity of the cathode material. Instead of the theoretical amount shown in the graphics, actual mass of the active materials are used for the capacity calculations. Comparison of the results are done by using capacity(x) vs. potential(y)

and cycles(x) vs. capacity(y) graphics. Highest capacity of each cycle for charging processes and the lowest capacity of each cycle while discharging processes are also compared.

### 5.5.1 Determination of the optimum carbon percentage for the cathode materials in the batteries prepared using $\text{LiPF}_6$ electrolyte solutions

Highest capacity value observed for the batteries prepared with 10% C/ $\text{Li}_2\text{MnSiO}_4$  and  $\text{LiPF}_6$  (EC:DEC) electrolyte solution was 32.0 mAh/g while the highest capacity value was 65.3 mAh/g for the batteries containing 10% C/ $\text{Li}_2\text{MnSiO}_4$  and  $\text{LiPF}_6$  (EC:DMC) electrolyte solution (Figure 5.20. and Figure 5.21.). According to the results  $\text{LiPF}_6$  (EC:DMC) electrolyte solution provided a better performance than  $\text{LiPF}_6$  (EC:DEC) for the batteries prepared with 10% C/ $\text{Li}_2\text{MnSiO}_4$ .

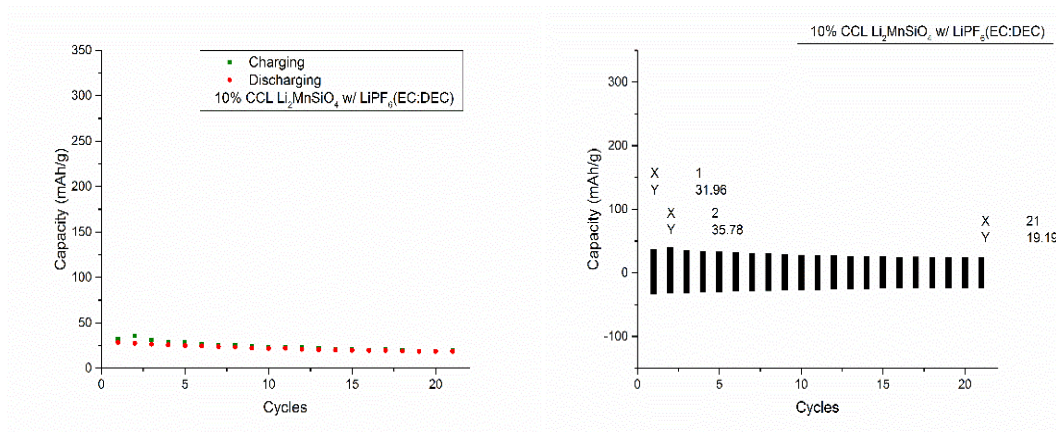


Figure 5.20. Comparison graphics of batteries containing 10% C/ $\text{Li}_2\text{MnSiO}_4$  and  $\text{LiPF}_6$ (EC:DEC).

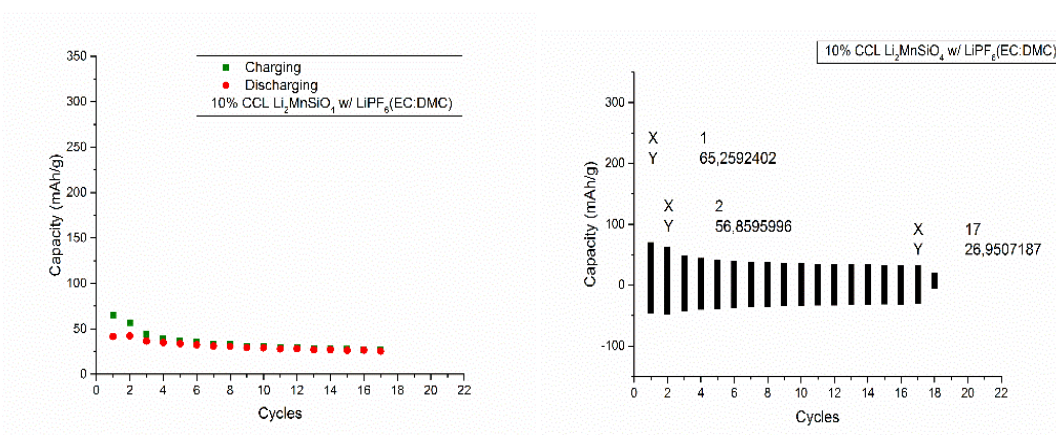
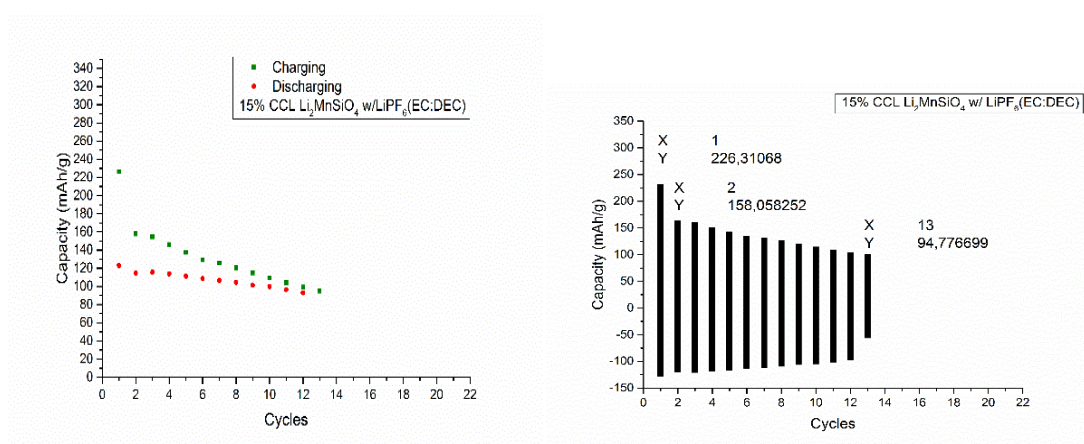


Figure 5.21. Comparison graphics of batteries containing 10% C/ $\text{Li}_2\text{MnSiO}_4$  and  $\text{LiPF}_6$ (EC:DMC).

Consequently, observed charge-discharge performances were much lower than the expectations for the batteries prepared with 10% C/Li<sub>2</sub>MnSiO<sub>4</sub>.

Highest capacity value observed for the batteries prepared with 15% C/Li<sub>2</sub>MnSiO<sub>4</sub> and LiPF<sub>6</sub> (EC:DEC) electrolyte solution was 226.3 mAh/g while the highest capacity value was 233.1 mAh/g for the batteries containing 15% C/Li<sub>2</sub>MnSiO<sub>4</sub> and LiPF<sub>6</sub> (EC:DMC) electrolyte solution (Figure 5.22. and Figure 5.23.). According to the results both of the electrolyte solutions provided similar performances for the batteries prepared with 15% C/Li<sub>2</sub>MnSiO<sub>4</sub>. Even though the observed charge-discharge performances were much better than that of the batteries prepared with 10% C/Li<sub>2</sub>MnSiO<sub>4</sub>, performances were still lower than the expectations.



**Figure 5.22.** Comparison graphics of batteries containing 15% C/Li<sub>2</sub>MnSiO<sub>4</sub> and LiPF<sub>6</sub>(EC:DEC).

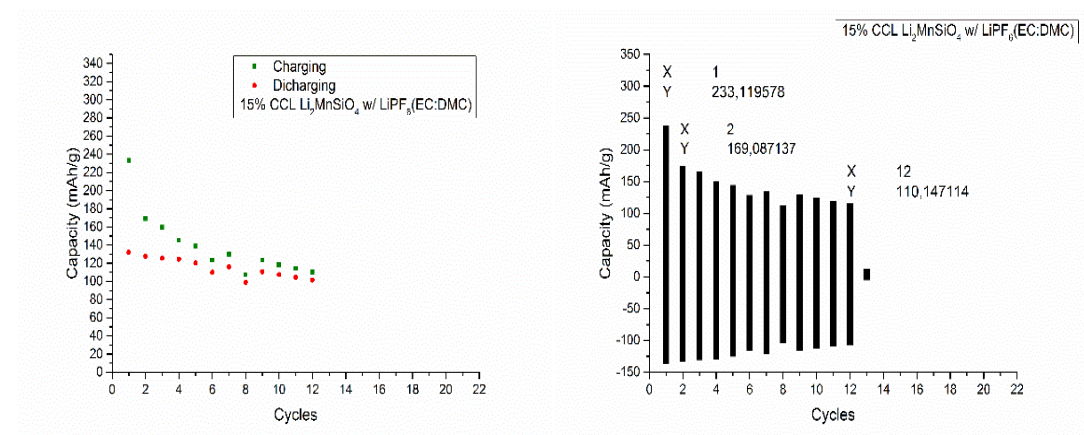


**Figure 5.23.** Comparison graphics of batteries containing 15% C/Li<sub>2</sub>MnSiO<sub>4</sub> and LiPF<sub>6</sub>(EC:DMC).

Highest capacity value observed for the batteries prepared with 20% C/Li<sub>2</sub>MnSiO<sub>4</sub> and LiPF<sub>6</sub> (EC:DEC) electrolyte solution was 129.4 mAh/g while the highest capacity value was 167.9 mAh/g for the batteries containing 20% C/Li<sub>2</sub>MnSiO<sub>4</sub> and LiPF<sub>6</sub> (EC:DMC) electrolyte solution (Figure 5.24. and Figure 5.25.). According to the results LiPF<sub>6</sub> (EC:DMC) electrolyte solution provided a better performance than LiPF<sub>6</sub> (EC:DEC) for the batteries prepared with 20% C/Li<sub>2</sub>MnSiO<sub>4</sub>. Consequently, observed charge-discharge performances were also much lower than the expectations for the batteries prepared with 20% C/Li<sub>2</sub>MnSiO<sub>4</sub>.

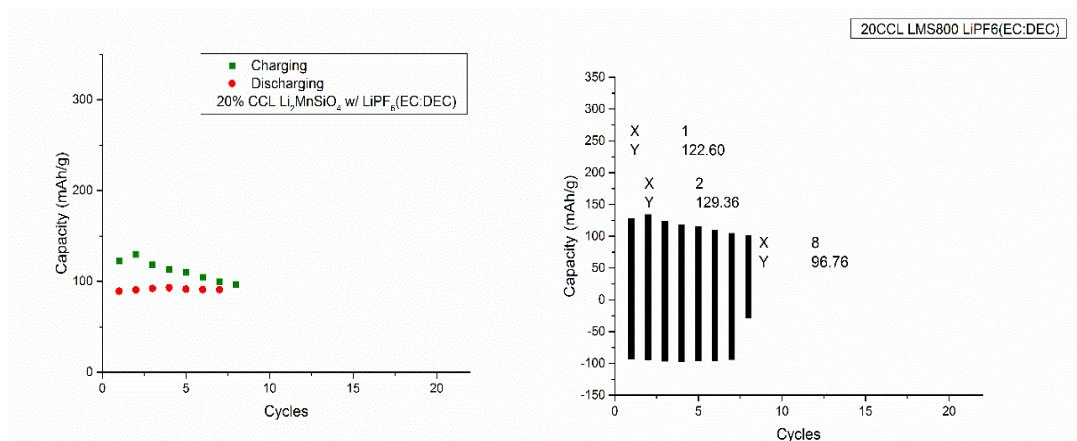


**Figure 5.24.** Comparison graphics of batteries containing 20% C/Li<sub>2</sub>MnSiO<sub>4</sub> and LiPF<sub>6</sub>(EC:DEC).

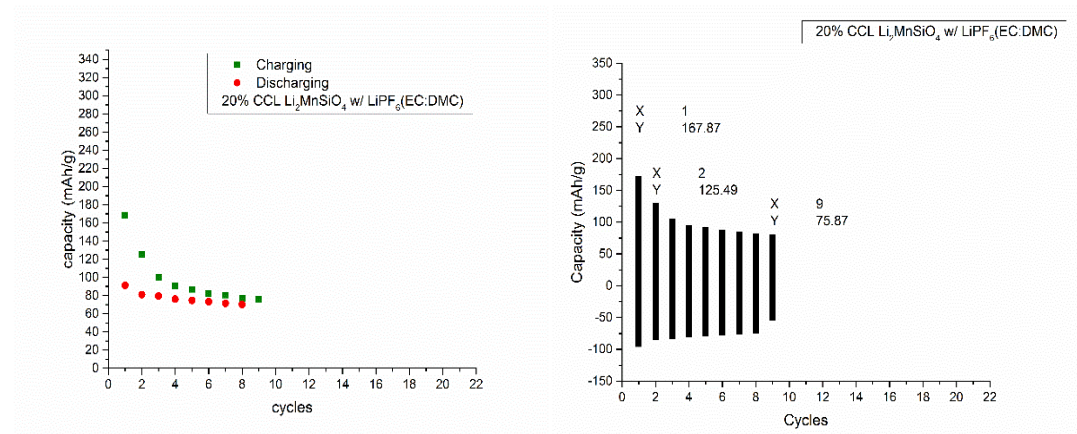


**Figure 5.25.** Comparison graphics of batteries containing 20% C/Li<sub>2</sub>MnSiO<sub>4</sub> and LiPF<sub>6</sub>(EC:DMC).

Highest capacity value observed for the batteries prepared with 25% C/Li<sub>2</sub>MnSiO<sub>4</sub> and LiPF<sub>6</sub> (EC:DEC) electrolyte solution was 293.6 mAh/g while the highest capacity value was 331.9 mAh/g for the batteries containing 25% C/Li<sub>2</sub>MnSiO<sub>4</sub> and LiPF<sub>6</sub> (EC:DMC) electrolyte solution (Figure 5.26. and Figure 5.27.). According to

the results  $\text{LiPF}_6$  (EC:DMC) electrolyte solution provided a better performance than  $\text{LiPF}_6$  (EC:DEC) for the batteries prepared with 25% C/ $\text{Li}_2\text{MnSiO}_4$ . Even though the observed charge-discharge performances of the first cycles were very close to the expectations for the batteries prepared with 25% C/ $\text{Li}_2\text{MnSiO}_4$ , cell capacity decreased severely during the next cycles.

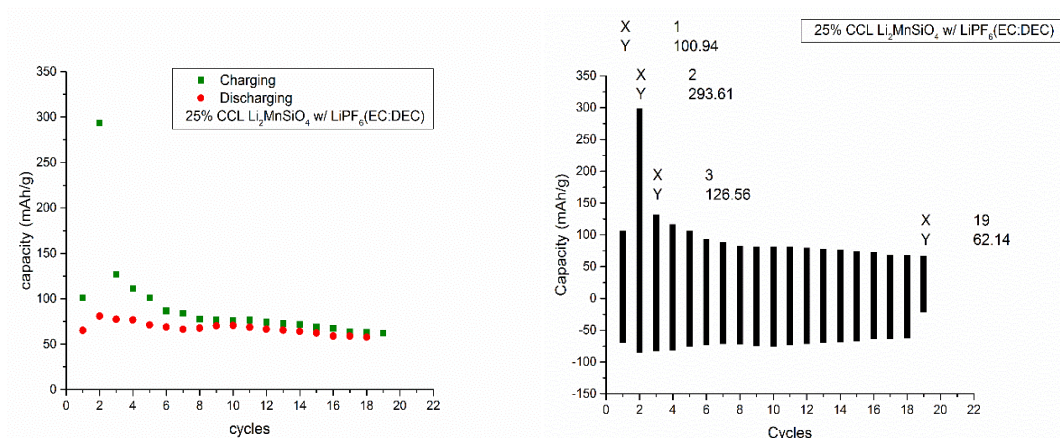


**Figure 5.26.** Comparison graphics of batteries containing 25% C/ $\text{Li}_2\text{MnSiO}_4$  and  $\text{LiPF}_6$ (EC:DEC).

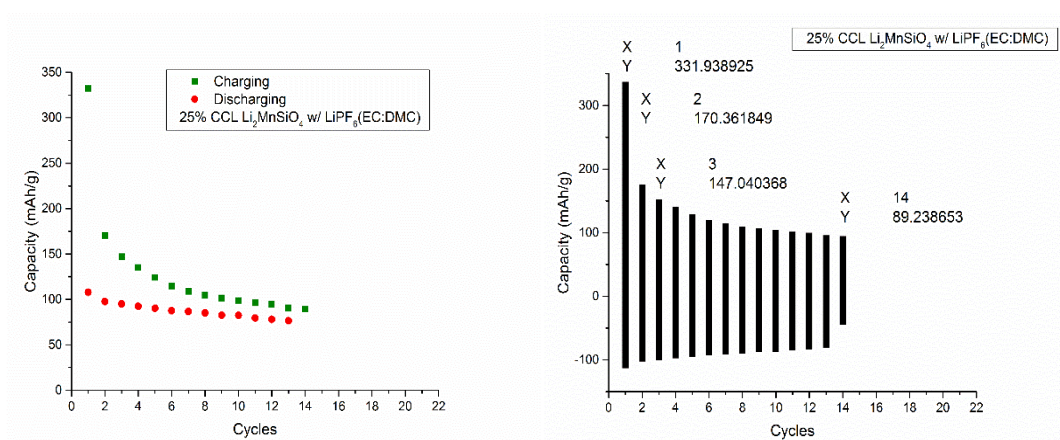


**Figure 5.27.** Comparison graphics of batteries containing 25% C/ $\text{Li}_2\text{MnSiO}_4$  and  $\text{LiPF}_6$ (EC:DMC).

Highest capacity value observed for the batteries prepared with 30% C/ $\text{Li}_2\text{MnSiO}_4$  and  $\text{LiPF}_6$  (EC:DEC) electrolyte solution was 340.0 mAh/g while the highest capacity value was 294.0 mAh/g for the batteries containing 30% C/ $\text{Li}_2\text{MnSiO}_4$  and  $\text{LiPF}_6$  (EC:DMC) electrolyte solution (Figure 5.28. and Figure 5.29.). Even though the charge-discharge performances of the first cycles were very close to the expectations for the batteries prepared with 30% C/ $\text{Li}_2\text{MnSiO}_4$ , cell capacities severely decreased during the next cycles.

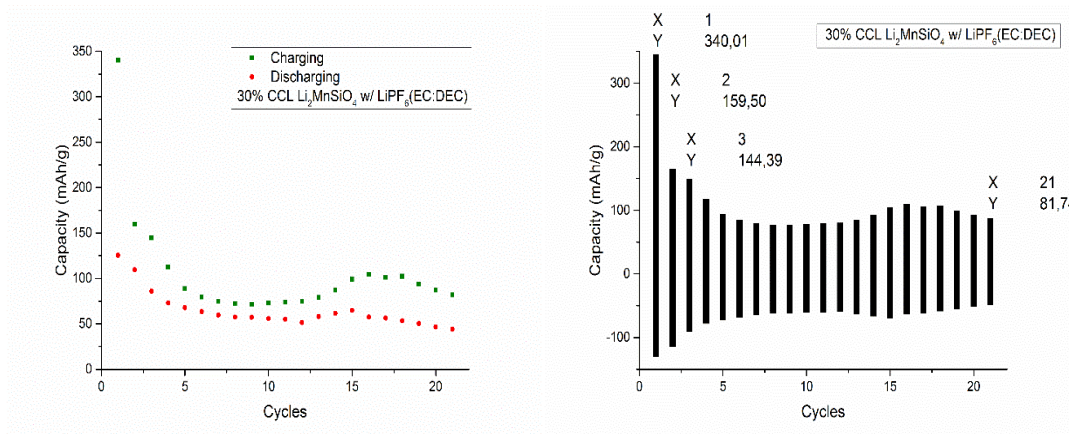


**Figure 5.28.** Comparison graphics of batteries containing 30% C/Li<sub>2</sub>MnSiO<sub>4</sub> and LiPF<sub>6</sub>(EC:DEC).

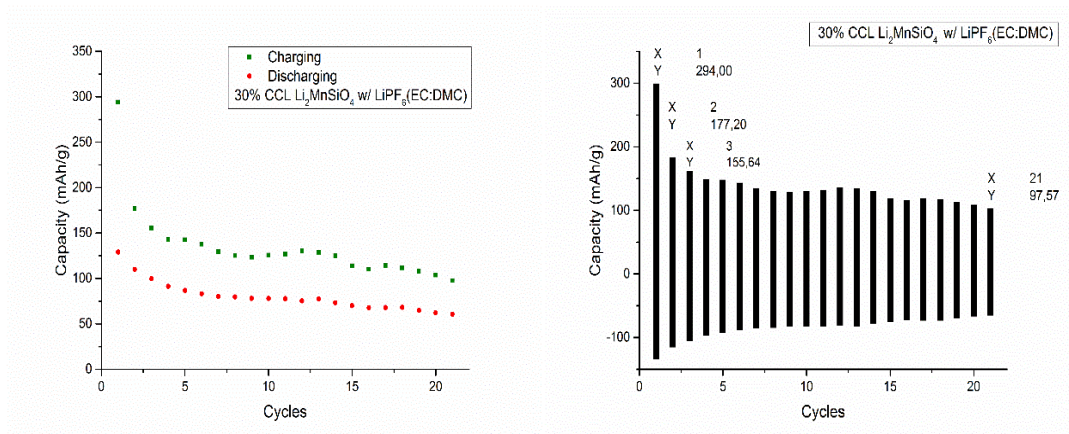


**Figure 5.29.** Comparison graphics of batteries containing 30% C/Li<sub>2</sub>MnSiO<sub>4</sub> and LiPF<sub>6</sub>(EC:DMC).

It is observed from the charge-discharge performance comparison of the batteries that, cell capacities are increased with the increase in the carbon content of the cathode material (Li<sub>2</sub>MnSiO<sub>4</sub>) in the cells. As a result, 30% is determined as the optimum carbon content for the cathode materials and 30% C/Li<sub>2</sub>MnSiO<sub>4</sub> is used for comparison of the performances of electrolyte solutions (Table 5.5.).

**Table 5.5.** Carbon contents vs. highest observed capacities

Carbon Content (%)	10	15	20	25	30
Highest Charging Capacity (mAh/g)	65.3	233.1	167.9	331.9	340.0
Highest Discharging Capacity (mAh/g)	49.7	122.5	71.56	82.4	147.0

## 5.5.2 Comparison of the electrolyte solution performances

Charge-discharge performances are compared for batteries prepared by using the electrolyte solutions shown in the Table 4.1, except for the electrolytes containing LiBOB due to the dissolution problems.

All of the batteries prepared by using the electrolyte solutions containing lithium bis(trifluoromethanesulfonyl)imide (LiTFSI) salt showed very high performances for the first cycles while galvanostatic charge-discharge tests, but the battery capacities decreased dramatically starting from the second cycle. Thus it is possible to say that, high capacities observed during the first cycles are a result of an undesired reaction in the cells and do not represent the lithiation/delithiation capacity of the  $\text{Li}_2\text{MnSiO}_4$  in the batteries (Figure 5.30.). As a result it is now known that the electrolyte solutions containing LiTFSI salt, used in this study, are not appropriate to be used for the batteries in which  $\text{Li}_2\text{MnSiO}_4$  is used as the cathode material.

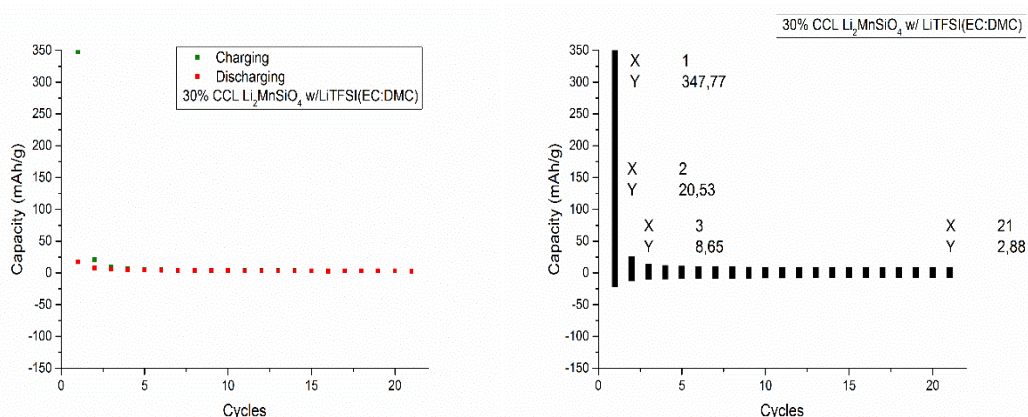


**Figure 5.30.** An example for the batteries prepared using 30% C/ $\text{Li}_2\text{MnSiO}_4$  cathode material and an electrolyte solution containing LiTFSI salt.

When the electrolyte solutions which are prepared by using lithium perchlorate ( $\text{LiClO}_4$ ) salt are compared, both  $\text{LiClO}_4(\text{EC}:\text{DMC})$  and  $\text{LiClO}_4(\text{TMS}:\text{EMC})$  showed poor performances during the galvanostatic charge-discharge tests while  $\text{LiClO}_4(\text{EC}:\text{DEC})$  showed a relatively better performance (Figure 5.31.).

Performance comparison of the electrolyte solutions containing lithium hexafluorophosphate ( $\text{LiPF}_6$ ) salt have proved that,  $\text{LiPF}_6(\text{TMS}:\text{EMC})$  showed the poorest performance during the galvanostatic charge-discharge tests. Furthermore, despite of its lower capacity at the first charge-discharge cycle,  $\text{LiPF}_6(\text{EC}:\text{DMC})$

showed a slightly better performance than  $\text{LiPF}_6(\text{EC}:\text{DEC})$  for the rest of the charge-discharge cycles (Table 5.6).

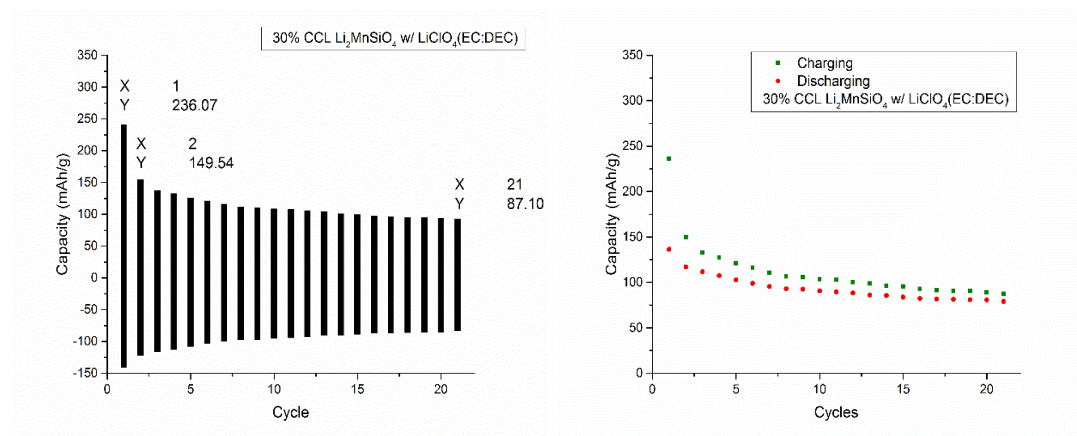


**Figure 5.31.** Comparison graphics of batteries containing 30% CCL  $\text{Li}_2\text{MnSiO}_4$  and  $\text{LiClO}_4(\text{EC}:\text{DEC})$ .

**Table 5.6.** Capacity values of the batteries prepared using different electrolyte solutions

Electrolyte Solution	Charging capacity of the 1 <sup>st</sup> cycle	Discharging capacity of the 1 <sup>st</sup> cycle	Charging capacity of the 21 <sup>st</sup> cycle
$\text{LiTFSI}(\text{EC}:\text{DEC})$	291.8 mAh/g	17.8 mAh/g	3.6 mAh/g
$\text{LiTFSI}(\text{EC}:\text{DMC})$	347.8 mAh/g	15.4 mAh/g	2.9 mAh/g
$\text{LiTFSI}(\text{TMS}:\text{EMC})$	528.5 mAh/g	29.1 mAh/g	10.2 mAh/g
$\text{LiPF}_6(\text{EC}:\text{DEC})$	340.0 mAh/g	91.6 mAh/g	81.7 mAh/g
$\text{LiPF}_6(\text{EC}:\text{DMC})$	294.0 mAh/g	147.0 mAh/g	97.6 mAh/g
$\text{LiPF}_6(\text{TMS}:\text{EMC})$	158.1 mAh/g	142.4 mAh/g	68.1 mAh/g
$\text{LiClO}_4(\text{EC}:\text{DEC})$	236.1 mAh/g	122.8 mAh/g	87.1 mAh/g
$\text{LiClO}_4(\text{EC}:\text{DMC})$	72.7 mAh/g	31.6 mAh/g	10.4 mAh/g
$\text{LiClO}_4(\text{TMS}:\text{EMC})$	109.5 mAh/g	79.9 mAh/g	45.6 mAh/g

In conclusion galvanostatic charge-discharge tests proved that,  $\text{LiPF}_6(\text{EC}:\text{DEC})$  and  $\text{LiClO}_4(\text{EC}:\text{DEC})$  electrolyte solutions showed similar performances to each other

and better performances from the other electrolyte solutions; while the highest stability as well as the best performance is observed for the  $\text{LiPF}_6(\text{EC}:\text{DMC})$  electrolyte solution.

### 5.5.3 XPS result of the fully charged cathode material

Average oxidation state of manganese (Mn) is calculated as 3.80 from XPS analysis of  $\text{Li}_2\text{MnSiO}_4$  particles after the first charging process (Table 5.7.). According to this result, most of the Mn species are on the fourth oxidation state while some Mn species also exist on the second oxidation state after the battery is completely charged. In conclusion it can be said that, electrochemical oxidation/delithiation of both of the lithiums from the cathode material ( $\text{Li}_2\text{MnSiO}_4$ ) is possible with the galvanostatic process.

**Table 5.7.** XPS information of electrochemically oxidized  $\text{Li}_2\text{MnSiO}_4$

Sample	Mn 3s			Oxidation State
	BE (1)	BE (2)	$\Delta E$	
30% CCL $\text{Li}_2\text{MnSiO}_4$ after charging process	75.99	80.62	4.6	3.80

### 5.6 DSC Results

Heat flow is examined related to the temperature change for 9 electrolyte solutions using differential scanning calorimetry (DSC) analyses in order to examine reactivity of solutions towards the  $\text{Li}_2\text{MnSiO}_4$  cathode material. Endothermic effects are observed around  $100^\circ\text{C}$  (related to EMC, DEC & DMC) and around  $260^\circ\text{C}$  (related to EC & TMS) for each sample due to evaporation of the solvents. Even though  $\text{LiClO}_4(\text{TMS}:\text{EMC})$  showed the optimum reactivity with the cathode material, salt decomposition is observed above  $300^\circ\text{C}$  for all electrolyte solutions containing  $\text{LiClO}_4$ . Along with the salt decomposition; a big exothermic effect, related to explosive behavior of the electrolyte solutions, is also observed for each solution containing  $\text{LiClO}_4$  salt. As a result it is proved that;  $\text{LiClO}_4(\text{EC}:\text{DMC})$ ,  $\text{LiClO}_4(\text{EC}:\text{DEC})$  and  $\text{LiClO}_4(\text{TMS}:\text{EMC})$  are not appropriate electrolyte solutions for Li-ion batteries (Figure 5.32.). Relatively better stabilities are observed for the electrolyte solutions containing LiTFSI salt, among which  $\text{LiTFSI}(\text{TMS}:\text{EMC})$  showed the best stability in the  $25^\circ\text{C} - 450^\circ\text{C}$  temperature interval (Figure 5.33.).

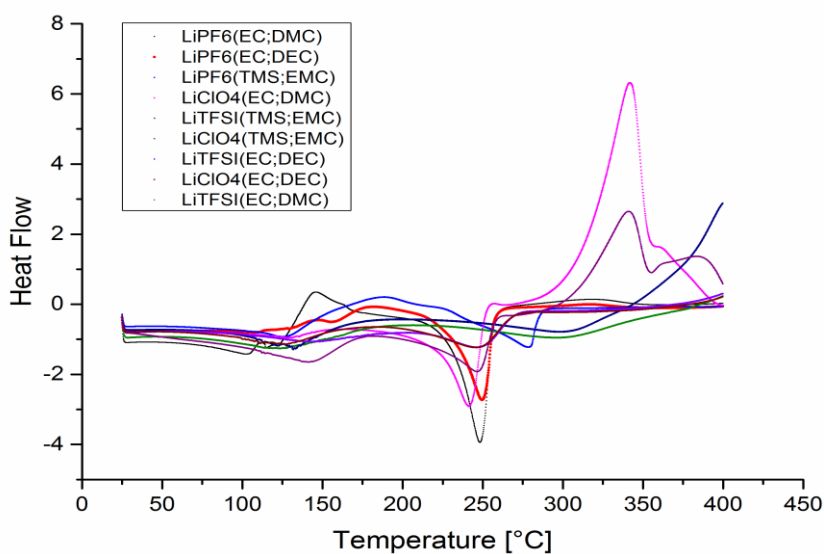


**Figure 5.32.** DSC comparison of the electrolyte solutions.

Afterwards, decomposition reactions of the electrolyte solutions under both argon and air atmospheres are examined by DSC analyses. According to the results, electrolyte decompositions were very similar under air and argon atmosphere for all of the electrolyte solutions. It is also observed that, evaporation of almost all solvents starts at slightly lower temperatures when the solutions are in contact with the cathode material. Furthermore it is observed for the solutions containing  $\text{LiClO}_4$  that, exothermic effect is increasing in case of the interaction of electrolyte solutions with  $\text{Li}_2\text{MnSiO}_4$ . Thus it can be said that, these electrolyte solutions are reactive towards the  $\text{Li}_2\text{MnSiO}_4$  cathode material.

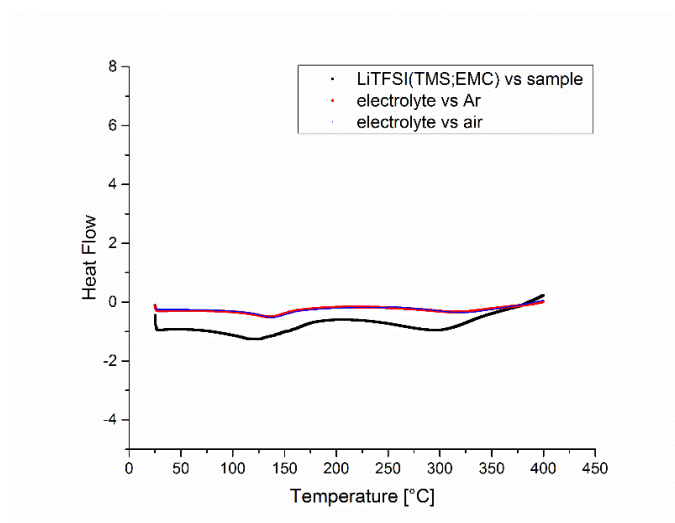


**Figure 5.33.** Degradation graphic of the most stable electrolyte solution.

## 6. CONCLUSIONS

XRD patterns of the pristine  $\text{Li}_2\text{MnSiO}_4$  and  $\text{C}/\text{Li}_2\text{MnSiO}_4$  composites proved that, Pechini type sol-gel synthesis is a convenient method to produce  $\text{Li}_2\text{MnSiO}_4$  and  $\text{C}/\text{Li}_2\text{MnSiO}_4$  nanoparticles. Crystallite sizes of the nanoparticles varied between 20 – 70 nm and the average crystallite size is calculated as 45 nm.

TG analyses proved that, water impregnation process is convenient to coat  $\text{Li}_2\text{MnSiO}_4$  nanoparticles precisely with the desired amount of conductive carbon layer. It is also observed from the XRD patterns that, water impregnation process do not cause a damage or change the structure of  $\text{Li}_2\text{MnSiO}_4$  nanoparticles.

Even though active material percentage in the 30%  $\text{C}/\text{Li}_2\text{MnSiO}_4$  nanoparticles is relatively lower due to the increasing amount of carbon and amount of adsorbed water on the carbon layer, cells containing 30%  $\text{C}/\text{Li}_2\text{MnSiO}_4$  composite cathode material showed the optimum performance during the galvanostatic charge-discharge tests. This situation can be explained with the directly proportional relationship of carbon percentages and conductivities since conductivity is increased with the increase in the carbon amount of  $\text{C}/\text{Li}_2\text{MnSiO}_4$  nanocomposites.

Average oxidation state of manganese in the electrochemically oxidized 30%  $\text{C}/\text{Li}_2\text{MnSiO}_4$  nanocomposites, taken from the completely charged battery, is calculated as 3.8. Thus it is possible to say that, most of Mn exist in the 4<sup>th</sup> state, along with a small amount of Mn on the 2<sup>nd</sup> and 3<sup>rd</sup> states, proving that both lithium ions could be delithiated from the cathode material. Since complete delithiation of 2 lithium ions from the  $\text{C}/\text{Li}_2\text{MnSiO}_4$  nanoparticles is possible, reversible exchange of up to two lithium ions per formula unit can be proved by examining the material after further discharging and charging processes.

According to the DSC measurements, electrolyte solutions prepared with  $\text{LiClO}_4$  salts are not appropriate to be used for the lithium ion batteries containing  $\text{Li}_2\text{MnSiO}_4$  cathode material, because of their explosive behavior. Furthermore it is observed that, electrolyte solutions containing LiTFSI salt are relatively more stable

towards C/Li<sub>2</sub>MnSiO<sub>4</sub> than the other electrolyte solutions while LiPF<sub>6</sub>(TMS:EMC) electrolyte solution also showed a good stability. However best practical capacities are observed for the cells containing LiPF<sub>6</sub>(EC:DMC), LiPF<sub>6</sub>(EC:DEC) and LiClO<sub>4</sub>(EC:DEC) electrolyte solutions during the galvanostatic charge-discharge tests. As a result it can be said that, despite of their good stabilities neither of the LiTFSI(EC:DEC), LiTFSI(EC:DMC), LiTFSI(TMS:EMC) and LiPF<sub>6</sub>(TMS:EMC) electrolyte solutions have a wide enough electrochemical window for this study in consideration of the required voltage range (1.5 – 4.8V) for delithiation of both lithium ions from the structure.

All of the reactions, except the 30 minute long heat treatment and reactions with K<sub>2</sub>S<sub>2</sub>O<sub>8</sub> for 24 hours and with NH<sub>3</sub> for 24 hours, caused a structure change or amorphisation for the cathode material. XPS analysis after the 30 minutes long heat treatment of Li<sub>2</sub>MnSiO<sub>4</sub> showed that, most of the the Mn is still on the 2<sup>nd</sup> oxidation state after the reaction thus the process is not useful to prove the reversible chemical lithiation/delithiation for the cathode material. Average oxidation state of manganese in Li<sub>2</sub>MnSiO<sub>4</sub> is calculated as 2.3 after the reaction with NH<sub>3</sub> for 24 hours and 2.5 after the reaction with K<sub>2</sub>S<sub>2</sub>O<sub>8</sub> for 24 hours. Thus it can be concluded that, some amount of Mn exists in 3<sup>rd</sup> and 4<sup>th</sup> oxidation state after reaction of the cathode material with K<sub>2</sub>S<sub>2</sub>O<sub>8</sub>.

## 7. REFERENCES

- [1] **Dubpernell, G. and Westbrook, J. H. (1978).** Proceedings of the Symposium on Selected Topics in the History of Electrochemistry. Princeton, NJ: *Electrochemical Society*. Print.
- [2] **Scrosati, Bruno. (2011).** "History of Lithium Batteries." *Journal of Solid State Electrochemistry* (15.7-8): 1623-630. Web.
- [3] **Padhi, A.K., Nanjundaswamy, K.S. and Goodenough J.B. (1997).** "Phospho-olivines as Positive-Electrode Materials for Rechargeable Lithium Batteries." *Journal of the Electrochemical Society* (144.4):1188. Web.
- [4] **Dell, R. and Rand, D. A. J. (2001).** Understanding Batteries. Cambridge: *Royal Society of Chemistry*. Print.
- [5] **Meyer, W.H. (1998).** Polymer Electrolytes for Lithium-Ion Batteries, *Advanced Materials* (10): 439-448, Web.
- [6] **Shapley Patricia. (2014).** *Common Battery Types*, [online] Available at <http://butane.chem.uiuc.edu/pshapley/GenChem2/C6/3.html>, (Accessed 4.11.2014).
- [7] **Flipsen, S.F.J. (2006).** Power Sources Compared: The Ultimate Truth?, *Journal of Power Sources* (162): 927. Web.
- [8] **Reinhardt Wagner. (2014).** Battery Fuel Gauges: Accurately Measuring Charge Level, [online] Available at <http://www.maximintegrated.com/app-notes/index.mvp/id/3958>, (Accessed 4.11.2014).
- [9] **Yanz, J. L., Ellessor, J. and Kaempff, H. (2012).** Bringing Rechargeable Hearing Aids into the Mainstream Market *Hearing Review* 19 (01): 28-31.
- [10] **Linden, D. and Reddy, T. B. (2002).** *Handbook of Batteries 3rd Edition*, chapter 22.
- [11] **Marshall Brain. (2006).** "How Lithium-ion Batteries Work 2006. [online] Available at HowStuffWorks.com, <http://electronics.howstuffworks.com/everyday-tech/lithium-ion-battery.htm>, (Accessed 15-04-2014).
- [12] **Ying Wang and Guozhong Cao. (2008).** Developments in Nanostructured Cathode Materials for High-Performance Lithium-Ion Batteries, *Advanced Materials*, Vol. 20, Issue 12.
- [13] **Janina Molenda and Marcin Molenda (2011).** Composite Cathode Material for Li-Ion Batteries Based on LiFePO<sub>4</sub> System., Metal, Ceramic and Polymeric Composites for Various Uses, Dr. John Cuppoletti (Ed.). Print.
- [14] **Molenda, M., Swietoslowski, M., Rafalska-Lasocha, A. and Dziembaj, R. (2011).**

C/Li<sub>2</sub>MnSiO<sub>4</sub> Nanocomposite Cathode Material for Li-Ion Batteries, *Funct. Mater. Lett.* (4): 135-138.

- [15] *Differential Scanning Calorimetry (DSC) and Thermogravimetric Analysis (TGA)*, [online] Available at [http://radchem.nevada.edu/classes/chem455/lecture\\_22\\_thermal\\_methods.htm](http://radchem.nevada.edu/classes/chem455/lecture_22_thermal_methods.htm), (Accessed 18-4-2014).
- [16] Lang, R., de Menezes, A. S., dos Santos, A. O., Reboh, S., Menezes, E. A., Amaral, L. and Cardoso, L. P. (2010). Ion-Beam-Induced Epitaxial Recrystallization Method and Its Recent Applications, *Crystal Growth & Design* (10): 4363.
- [17] Van der Heide, Paul, (2011). X-ray Photoelectron Spectroscopy: An introduction to Principles and Practices, Wiley, Print.
- [18] Engelhard, Mark, *X-Ray Photoelectron Spectroscopy XPS*, [online] Available at [http://www.emsl.pnl.gov/capabilities/spectroscopy/engelhard\\_xps.pdf](http://www.emsl.pnl.gov/capabilities/spectroscopy/engelhard_xps.pdf), (Accessed 19-04-2014)
- [19] Radiometer Analytical SAS, *Conductivity Theory and Practice*, [online] Available at [http://www.analytical-chemistry.uoc.gr/files/items/6/618/agwgimometria\\_2.pdf](http://www.analytical-chemistry.uoc.gr/files/items/6/618/agwgimometria_2.pdf), (Accessed 19-04-2014).
- [20] Molenda, M., Dziembaj, R., Kochanowski, A., Bortel, E., Drozdek, M. and Piwowarska, Z. (2010). Process for the Preparation of Conductive Carbon Layers on Powdered Supports, Int. Patent App. No. WO 2010/021557, US Patent Application 20110151112.
- [21] Molenda, M., Dziembaj, R., Drozdek, M., Podstawka, E. and Proniewicz, L. M. (2008). Direct Preparation of Conductive Carbon Layer (CCL) on Alumina as a Model System for Direct Preparation of Carbon Coated Particles of the Composite Li-ion Electrodes, *Solid State Ionics* (179): 197-201.
- [22] Marcin Molenda, Michal Świątosławski and Roman Dziembaj. (2012). C/Li<sub>2</sub>MnSiO<sub>4</sub> Nanocomposite Cathode Material for Li-Ion Batteries, *Composites and Their Properties* chapter 4, Ning Hu (eds.).
- [23] Dominko et al. (2006). Structure and Electrochemical Performance of Li<sub>2</sub>MnSiO<sub>4</sub> and Li<sub>2</sub>FeSiO<sub>4</sub> as Potential Li-battery Cathode Materials, *Electrochemistry Communications* (8): 217-222.
- [24] Kalantarian, M. M., Asgari S., Mustarelli P. (2013). Theoretical Investigation of Li<sub>2</sub>MnSiO<sub>4</sub> as a Cathode Material for Li-ion Batteries: a DFT study, *J. Mater. Chem. A* (1): 2847.
- [25] Verma, P., Maire, P. and Novák, P. (2010). A Review of the Features and Analyses of the Solid Electrolyte Interphase in Li-ion Batteries, *Electrochimica Acta* (55): 6332–6341.
- [26] Xu, Kang (2004). Nonaqueous Liquid Electrolytes for Lithium-based Rechargeable Batteries, *Chem. Rev.* (104): 4303-4417.
- [27] Scrosati, Bruno. (2000). Recent Advances in Lithium Ion Battery Materials, *Electrochimica Acta* (45): 2461–2466.

- [28] **Amatucci, G. C., Schmutz, C. N., Blyr, A., Sigala, C., Gozdz, A. S., Larcher, D. and Tarascon, J. M. (1997).** *J. Power Sources* (69): 11.
- [29] **Xu Kang et al. (2002).** Lithium Bisoxalatoborate Stabilizes Graphite Anode in Propylene Carbonate, *Electrochemical and Solid-State Letters* 5 (11): 259-262.
- [30] **Sheng Shui Zhang. (2006).** A Unique Lithium Salt for the Improved Electrolyte of Li-ion Battery, *Electrochemistry Communications* 8, 1423–1428.
- [31] **Matsuda, Y. (1985).** Characteristics of Sulfolane-based Electrolytes for Rechargeable Lithium Batteries, *J. Electrochem. Soc.* 132 (11): 2538-2543.
- [32] **Aurbach, D. et al. (2004).** “Design of electrolyte solutions for Li and Li-ion batteries: a review.” *Electrochimica Acta* 50 (2-3): 247-54.
- [33] **Akbari, B. et al. (2011).** Particle Size Characterization of Nanoparticles – A Practical Approach. *Iranian Journal of Materials Science & Engineering* (8): 2.
- [34] **Birkbeck College, University of London. (2013).** *High-Resolution Space Group Diagrams and Tables*; [Online] Available at <http://img.chem.ucl.ac.uk/sgp/large/sgp.htm> (Accessed 12-12-2013).
- [35] **Amatucci, G. G. and Pereira, N. (2007).** *J. Fluorine Chem.*, 2007, 128, 243
- [36] **Amatucci, G. G. et al. (2010).** Formation, Dynamics, and Implication of Solid Electrolyte Interphase in High Voltage Reversible Conversion Fluoride Nanocomposites, *J. Mater. Chem.* (20): 4149-4161.
- [37] **Leclanché, G. L. (1866).** *Compt. Rend* (83): 54.
- [38] **Mizushima, K., Jones P. C., Wiseman P. J. and Goodenough J.B. (1981).** *Solid State Ionics*, (7): 314.
- [39] **Jahn, H. A. and Teller, E. (1937).** *Proc. R. Soc. London A*, (161): 220-235.
- [40] **Gaberscek M. et al. (2007).** Beyond One-Electron Reaction in Li Cathode Materials: Designing  $\text{Li}_2\text{Mn}_x\text{Fe}_{1-x}\text{SiO}_4$ , *Chem. Mater.* (19): 3633-3640.
- [41] **Gratzel M. et al. (2013).** Reversible Chemical Delithiation/lithiation of  $\text{LiFePO}_4$ : Towards a Redox Flow Lithium-ion Battery. *Phys.Chem. Chem. Phys.* (15): 1793-1797.



## CURRICULUM VITAE



**Name:** Ekin Eşen

**Date of birth:** 11.08.1990

**Permanent Address:** Eskişehir Mahallesi Aldamda Sokak Rüzgar Apt. No:19  
Kurtuluş, Şişli / İstanbul

### Education:

Fall 2012 – Spring 2015 **MSc in Nano Science And Nano Engineering**  
Istanbul Technical University  
Graduate School of Science Engineering and Technology  
Overall GPA: 3.44/4.00

Fall 2008 – Summer 2012 **BSc in Chemistry**  
Istanbul Technical University  
Faculty of Sciences and Letters  
Overall GPA: 2.79/4.00

### Exams

UDS (University language exam) result: 93.75/100 (English)

ALES (Academic Personnel and Postgraduate Education Exam) result: 88.7/100

### Awards:

The best oral presentation (English) Horizons of Science 2014 Forum of Diploma Thesis, Krakow, Poland.

### Work Experience:

Master Thesis Study under supervision of Dr. Marcin Molenda at Jagiellonian University in Krakow - Poland (Uniwersytet Jagiellonski w Krakowie), Department of Chemical Technology, Technology of Materials and Nanomaterials Research Group, 2013-2014 Academic year (Erasmus Exchange Program)

'Chemical Deintercalation and Stability Investigation of  $\text{Li}_2\text{MnSiO}_4$  Cathode Material with Different Electrolytes.'

Undergraduate Project under supervision of Prof. Dr. H. Huceste Giz at Istanbul Technical University Polymerization Kinetics Laboratory, 2011-2012 Academic year

'Determination of Equilibrium Constant for Neutralization Reaction of Poly-Diallyldimethylammonium Chloride.'

Industrial Internship at Simteks Toptan Tekstil Boya Pazarlama Sanayi ve Ticaret Limited Şirketi (Simteks Textile Paint Marketing Industry and Commerce Inc.), Summer 2012

Laboratory Internship at R&D department of Organik Kimya Sanayi ve Ticaret Anonim Şirketi (Organik Kimya Industry and Commerce Inc.), Summer 2011

Laboratory Internship under supervision of Prof. Dr. H. Huceste Giz at Istanbul Technical University Polymerization Kinetics Laboratory, Summer 2010

Tutoring high school students (Chemistry, Physics, Mathematics, Turkish) 2009 - 2015

#### **Experiences:**

- Worked as a member of professional research teams.
- Experienced working within an industrial factory.
- Learned and/or used X-ray Diffraction (XRD), Thermo-gravimetric analysis (TGA), Differential scanning calorimetry (DSC), Electrical conductivity measurements (EC), Galvanostatic charge-discharge tests, High performance liquid chromatography (HPLC), Ultraviolet-visible UV/Vis) spectrophotometer and Continuous data observing system (ACOMP).
- Learned the basic analyze techniques used for polymers (adhesive, paint and construction R&D Departments)

#### **Publications:**

- M. Świątosławski, M. Molenda\*, **Ekin Eşen**, R. Dziembaj, Searching for the Best Electrolyte Composition for the C/Li<sub>2</sub>MnSiO<sub>4</sub> Based Battery System, ECS Transactions, 62 (1) 89-96 (2014)

Activities:

ERASMUS exchange, 2013 – 2014 (Poland)

ITU Epgik Club, Illustrator, 2009 – 2011

ITU Dance and Gymnastic Club, 2008 – 2011 (Tango, Salsa, Greek Dance)

## References

Prof. Dr. Figen Kadirgan, Master's Thesis Advisor  
Istanbul Technical University, Department of Chemistry  
[kadirgan@itu.edu.tr](mailto:kadirgan@itu.edu.tr), Tel: +90 212 2856386

Dr. Marcin Molenda, Master's Thesis Advisor  
Jagiellonian University in Krakow, Department of Chemical Technologies  
[molendam@chemia.uj.edu.pl](mailto:molendam@chemia.uj.edu.pl), Tel: +48 12 663 2280

Dr. Michal Swietoslowski, Master's Thesis Co-advisor  
Jagiellonian University in Krakow, Department of Chemical Technologies  
[m.swietoslowski@uj.edu.pl](mailto:m.swietoslowski@uj.edu.pl)

Prof. Dr. H. Huceste Giz, Undergraduate Thesis Advisor  
Istanbul Technical University, Department of Chemistry  
[catalgil@itu.edu.tr](mailto:catalgil@itu.edu.tr), Tel: +90 212 2853279